Neutron Star Crusts

Paweł Haensel

N. Copernicus Astronomical Center, Polish Academy of Sciences,
Bartycka 18, PL-00-716 Warszawa, Poland

Abstract. The formation, structure, composition, and the equation of state of neutron star crusts are described. A scenario of formation of the crust in a newly born neutron star is considered and a model of evolution of the crust composition during the early neutron star cooling is presented. Structure of the ground state of the crust is studied. In the case of the outer crust, recent nuclear data on masses of neutron rich nuclei are used. For the inner crust, results of different many-body calculations are presented, and dependence on the assumed effective nucleon-nucleon interaction is discussed. Uncertainties concerning the bottom layers of the crust and crust-liquid interface are illustrated using results of various many-body calculations based on different effective nucleon-nucleon interactions. A scenario of formation of a crust of matter-accreting neutron star is presented, and evolution of the crust-matter element under the increasing pressure of accreted layer is studied. Within a specific dense matter model, composition of accreted crust is calculated, and is shown to be vastly different from the ground-state one. Non-equilibrium processes in the crust of mass-accreting neutron star are studied, heat release due to them is estimated, and their relevance to the properties of X-ray sources is briefly discussed. Equation of state of the ground-state crust is presented, and compared with that for accreted crust. Elastic properties of the crust are reviewed. Possible deviations from idealized models of one-component plasmas are briefly discussed.

1 Introduction

The crust plays an important role in neutron star evolution and dynamics. Its properties are crucial for many observational properties, despite the fact that the crust mass constitutes only $\sim 1\%$ of neutron star mass, and its thickness is typically less than one tenth of the star radius. The crust separates neutron star interior from the photosphere, from which X-ray radiation is emitted. The transport of heat from neutron star core to the star surface is determined by the thermal conductivity of the outer layers of the crust, which is crucial for determining the relation between observed X-ray flux and the temperature of neutron star core.

Electrical resistivity of the crust is expected to be important for the evolution of neutron star magnetic field. Both thermal conductivity and electrical resistivity depend on the structure of the crust, its nuclear composition, and the presence and number of crystalline defects and impurities. During some stages of neutron star cooling, neutrino emission from the crust may significantly contribute to total neutrino losses from stellar interior. The presence of a crystal

D. Blaschke, N.K. Glendenning, and A. Sedrakian (Eds.): LNP 578, pp. 127–174, 2001.

lattice of atomic nuclei in the crust is mandatory for modeling of radio–pulsar glitches. Presence of solid crust enables excitation of toroidal modes of oscillations. The toroidal modes in a completely fluid star have all zero frequency, but the presence of a solid crust gives them nonzero frequencies ∼kHz. Presence of the crust can also be important for non-radial pulsations excited in the liquid core, because of specific boundary conditions which are to be imposed at the solid-liquid boundary. Due to its solid character, neutron star crust can be a site of elastic stresses, and can build-up elastic strain during star evolution (cooling, spin-down). In contrast to fluid core, the crust can therefore support deviations of the stellar shape from the axial symmetry, and make from rapidly rotating pulsar an interesting source of gravitational waves. Instabilities in the fusion of light elements, taking place in the outer layers of the crust of an accreting neutron star, are thought to be responsible for the phenomenon of X-ray bursts.

The present review is devoted to the structure, composition, and equation of state of neutron star crust. In Sect.2 we briefly describe formation of the crust of a newly born neutron star. Structure, composition, and equation of state of the outer crust in the ground state approximation is described in Sect.3. Theoretical models of the inner crust in the ground state approximation and with $\rho \lesssim 10^{14}$ g cm^{-3} are presented in Sect. 4. Section 5 is devoted to the presentation of theoretical models of the ground state of the bottom layers of the inner crust, with $\rho \gtrsim 10^{14}$ g cm^{-3}, and to determination of the location of and conditions at the bottom edge of the crust. In Sect. 6 we consider a scenario of formation of the crust in accreting neutron star. Then, in Sect. 7 we study non-equilibrium nuclear processes in the crust interior, and derive its structure and nuclear composition. Sect. 8 is devoted to the equation of state of neutron star crust, both in the ground state approximation and in the case of an accreted crust. Elastic properties of the crust are discussed in Sect. 9. Possible deviations from idealized crust models studied in the preceding sections are briefly reviewed in Sect.10.

2 Formation of the crust in a newly born neutron star

Neutron star formed in gravitational collapse of a stellar core is initially very hot, with internal temperature $\sim 10^{11}$ K. At such high temperature, the composition and equation of state of the outer envelope of a newly-born neutron star, with $\rho \lesssim 10^{14}$ g cm^{-3} ($n_b \lesssim 0.1$ fm^{-3}), is different from that of a one-year old neutron star. This envelope of a newly-born neutron star will eventually become the crust of neutron star.

We will restrict ourselves to the case in which matter is transparent to neutrinos, a condition satisfied for $T \lesssim 10^{10}$ K ($k_{\rm B}T \lesssim 1$ MeV). Hot envelope is then a mixture of heavy and light nuclei (mostly α-particles, because of their large binding energy of 28.3 MeV), neutrons, protons, electrons, positrons, and photons. At high densities and temperatures the density of nucleons outside nuclei can be large, and a consistent treatment of both nuclei and nucleons is required. Nuclei and nucleons outside them should be described using the same

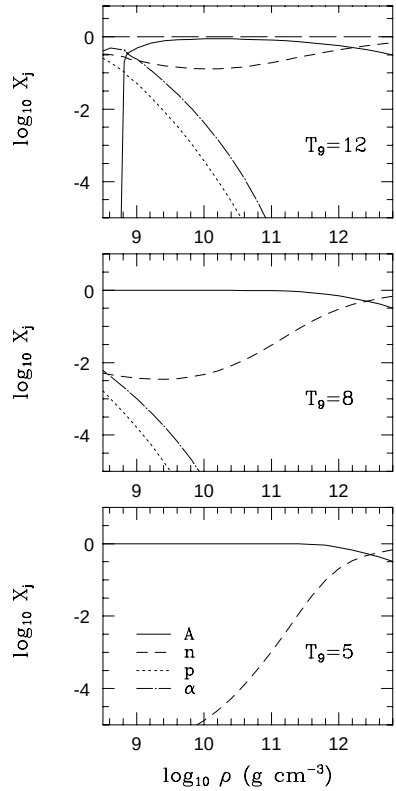

Fig. 1. Mass fractions of different constituents of the outer envelope of a newly born neutron star versus matter density, at different temperatures $T_9 = T/(10^9$ K). Beta equilibrium assumed. After Haensel et al. [40]. Calculations performed for the Lattimer and Swesty [53] model, with a specific choice of the compression modulus of cold symmetric nuclear matter at the saturation density, $K_0 = 180$ MeV.

nucleon interaction (nucleon hamiltonian), and modifications of nuclear surface properties, and pressure exerted by nucleons on nuclei, have to be calculated in a consistent way. At high densities, where the distance between nuclei is no longer much larger than nuclear size, one has to take into account modification of the nuclear Coulomb energy. Another important complication is that, at temperatures under consideration, excited states of nuclei become populated and must therefore be considered when calculating thermodynamic quantities.

In what follows, we will describe results, obtained using a version of compressible liquid–drop model of nuclei developed by Lattimer and Swesty [53], with a specific choice of compression modulus of symmetric nuclear matter at saturation (equilibrium) density, $K_0 = 180$ MeV. We assume nuclear equilibrium, as well as beta equilibrium of dense hot matter. The assumption of nuclear equilibrium is justified by high temperature. Beta equilibrium is adopted for simplicity;

a very rapid cooling of matter at highest temperatures can produce deviations from beta equilibrium.

In Fig.1 we show the composition of dense, hot matter of neutron star envelope for $T = 5 \times 10^9$ K, 8×10^9 K, and 1.2×10^{10} K. We restrict ourselves to $\rho \lesssim 10^{13}$ g cm^{-3}, because at higher densities thermal effects on matter composition are negligible. At $T \gtrsim 5 \times 10^9$ K shell and paring effects, so visible in the $T = 0$ approximation where they show up through jumps in the density dependence of various quantities, are washed out by the thermal effects.

At $T = 1.2 \times 10^{10}$ K nuclei evaporated completely for $\rho \lesssim 10^9$ g cm^{-3}. This can be understood within the compressible liquid-drop model of nuclei, which are treated as droplets of nuclear matter. At $\rho \lesssim 10^{11}$ g cm^{-3} these droplets of nuclear matter have to coexist with a vapor of neutrons, protons, and α–particles. However, coexistence of two different nucleon phases (denser – nuclear matter liquid, less dense – vapor of nucleons and α–particles) is possible only at T lower than critical temperature at given density, $T_{\rm crit}(\rho)$. For $\rho \lesssim 10^9$ g cm^{-3}, one has $T_{\rm crit}(\rho) < 1.2 \times 10^{10}$ K.

With decreasing temperature, mass fraction of evaporated nucleons and α–particles decreases. At $T = 8 \times 10^9$ K, α–particles are present below 10^{10} g cm^{-3}, while free protons appear below even lower density. Free neutrons are present at all densities, but their fraction does not exceed one percent for $\rho \lesssim 10^{11}$ g cm^{-3}.

At $T = 5 \times 10^9$ K the thermal effects are weak, and imply mainly appearance of a small fraction of free neutrons ("neutron vapor") below zero temperature neutron drip density, $\rho_{\rm ND}$; this fraction falls below 10^{-5} at $\rho = 10^{10}$ g cm^{-3}. Further decrease of T leads to disappearance of neutrons below $\rho_{\rm ND}$, and switching–on of shell effects. Another important effect will be superfluid transition for neutrons (both inside and outside nuclei) and for protons. The composition freezes–out and does not change with further decrease of temperature. A spherical shell of neutron star envelope solidifies if its temperature decreases below the melting point corresponding to local density and composition, $T_{\rm m}$ (see Sect.9).

3 Ground state of the matter in the outer crust

The ground state of matter at the densities and pressures, at which all neutrons are bound in nuclei (i.e. below the neutron drip point) can be described by a model formulated in the classical paper of Baym, Pethick, and Sutherland ([4], hereafter referred to as BPS). An essential input for this model are the ground-state masses of atomic nuclei, present in the lattice sites of a crystal. At lowest densities, the relevant nuclei are those whose ground-state masses are determined with high precision by the laboratory measurements. However, at higher densities the nuclei in the ground state of matter become more and more neutron rich. At the time, when the BPS paper was written, the last experimentally studied nucleus, present in the ground state of dense matter, was ^{84}Se ($Z/A = 0.405$). This nucleus is unstable in laboratory, and its beta-decay half-life time is 3.1 min. The maximum density, at which this experimentally studied nucleus was present, was found to be 8.2×10^9 g cm^{-3}.

During last two decades significant progress has been made in the experimental nuclear physics techniques, and masses of many new neutron rich isotopes have been measured; latest up-to-date results can be found at *http://nucleardata.nuclear.lund.se*. As we will see, the last neutron-rich nucleus studied in laboratory, which is expected to be present in the ground state of neutron star crust, is ^{78}Ni, at about 10^{11} g cm^{-3} (for first experimental identification of this nuclide, see Engelmann et al. [32])

We shall assume that matter is in its ground state (complete thermodynamic equilibrium - cold catalyzed matter) and that it forms a perfect crystal with a single nuclear species, (number of nucleons A, number of protons Z), at lattice sites. Deviations and exceptions from this rule will be discussed later in the present review. At given baryon density, $n_{\rm b}$, the ground state of matter corresponds to the minimum energy per nucleon $E = \mathcal{E}/n_{\rm b}$ ($\mathcal{E}$ is energy density, which includes rest energy of constituents of matter). However, $n_{\rm b}$ (or $\rho = \mathcal{E}/c^2$) is not a good variable to be used in the neutron star interior because it can suffer jumps (discontinuities) at some values of pressure. On the contrary, pressure is strictly monotonic and continuous in the stellar interior, and increases monotonically with decreasing distance from the star center. Therefore, it is convenient to formulate our problem as that of finding the ground state of cold ($T = 0$) matter at given pressure, P. This correspond to minimizing the $T = 0$ Gibbs energy per nucleon, $g = (\mathcal{E} + P)/n_{\rm b}$.

Let us start with $P = 0$, when $g = E = \mathcal{E}/n_{\rm b}$. The minimum energy per nucleon at zero pressure is reached for a body-centered-cubic (bcc) crystal lattice of ^{56}Fe, and is $E(^{56}\mathrm{Fe}) = 930.4$ MeV. It corresponds to $\rho = 7.86$ g cm^{-3} and $n_{\rm b} = 4.73 \times 10^{24}$ cm^{-3} $= 4.73 \times 10^{-15}$ fm^{-3}.

The bcc ^{56}Fe crystal remains the ground state of cold matter up to pressures $\sim 10^{30}$ dyn/cm^2, at which matter is compressed to $\sim 10^6$ g cm^{-3} ([81], BPS). At such a high density, matter is a plasma of nuclei and electrons which form a nearly uniform Fermi gas. At given pressure, the values of the average electron density, n_e, and the number density of nuclei, $n_{\mathcal{N}}$, are determined from the relations

$$n_e = Z n_{\mathcal{N}} \ , \qquad P = P_e(n_e, Z) + P_L(n_{\mathcal{N}}, Z) \ , \tag{1}$$

where P_e is the electron gas pressure, and $P_{\rm L}$ is the "lattice" contribution resulting from the Coulomb interactions (see below).

Let us divide the system into electrically neutral unit (Winger-Seine) cells containing one nucleus. The number density of nuclei is $n_{\mathcal{N}} = n_{\rm b}/A$, and the volume of each cell $V_{\rm c} = 1/n_{\mathcal{N}}$. For a given A, Z nuclide, the Gibbs energy per one unit cell is given by

$$G_{\rm cell}(A, Z) = W_{\mathcal{N}}(A, Z) + W_L(Z, n_{\mathcal{N}}) + [\mathcal{E}_e(n_e, Z) + P]/n_{\mathcal{N}} \ , \tag{2}$$

where $W_{\mathcal{N}}$ is the energy of the nucleus (including rest energy of nucleons), W_L is the lattice energy per cell (BPS), and $\mathcal{E}_e$ is the mean electron energy density.

For a bcc lattice one has

$$W_{\rm L} = -0.895929\ \frac{Z^2 e^2}{r_{\rm c}}, \qquad r_{\rm c} = (4\pi n_{\mathcal{N}}/3)^{-1/3}\ . \tag{3}$$

The lattice contribution to pressure, (1), is thus $P_{\rm L} = \frac{1}{3} W_{\rm L} n_{\mathcal{N}}$.

The Gibbs energy per nucleon $g = G_{\rm cell}/A$ is just the baryon chemical potential for a given nuclid, $\mu_{\rm b}(A, Z)$. To find the ground state at given P, one has to minimize $\mu_{\rm b}(A, Z)$ with respect to A and Z.

At not too high density, the lattice correction to P and $\mu_{\rm b}$ is negligibly small. One can then easily see the reason for matter neutronization using the approximation $\mu_{\rm b}(A, Z) \simeq W_{\mathcal{N}}(A, Z)/A + Z\mu_e/A$ and $P \simeq P_e$. Notice that for $\rho \gg 10^6$ g cm^{-3}, electrons are ultrarelativistic and therefore $\mu_e \propto P^{1/4}$. With increasing pressure, it is energetically advantageous to replace (A, Z) by (A', Z') with higher $W_{\mathcal{N}}$ but smaller Z'/A', because increase in $W_{\mathcal{N}}/A$ is more than compensated by the decrease of the $Z\mu_e/A$ term.

We will follow determination of the ground state of cold dense matter by Haensel and Pichon [39] (hereafter referred to as HP). There are some small differences between the approximations used in HP and BPS. In HP, the values of $W_{\mathcal{N}}$ have been obtained from the atomic masses by subtracting not only the electron rest energies, but also removing the atomic electron binding energies. Let us mention, that atomic binding energies were kept in the BPS definition of $W_{\mathcal{N}}$, to simulate the electron screening effects in dense matter. Also, HP used a better approximation for the electron screening effects in dense matter. Their expression for $\mathcal{E}_e$ takes into account deviations of the electron density from uniformity, which result from the electron screening effects. They include also the exchange term in $\mathcal{E}_e$, which was neglected in BPS.

At the pressure P_i at which optimal values A, Z change into A', Z', matter undergoes a density jump, $\Delta\rho$, $\Delta n_{\rm b}$, which to a very good approximation is given by the formula

$$\frac{\Delta\rho}{\rho} \cong \frac{\Delta n_{\rm b}}{n_{\rm b}} \cong \frac{Z}{A}\frac{A'}{Z'} - 1\ . \tag{4}$$

The above equation results from the continuity of pressure, which in the outer crust is to a very good approximation equal to the electron pressure, $P \simeq P_e$.

Actually, sharp discontinuity in ρ and $n_{\rm b}$ is a consequence of the assumed one-component plasma model. Detailed calculations of the ground state of dense matter by Jog and Smith [45] have shown, that the transition between the A, Z and A', Z' shells takes places through a very thin layer of a *mixed lattice* of these two species. However, since the pressure interval within which the mixed phase exists is typically $\sim 10^{-4} P_i$, the approximation of a sharp density jump is quite a good representation of a nuclear composition of the ground state of matter.

Experimental masses of nuclei in HP were taken from nuclear masses tables of Audi (1992, 1993, private communication) [1] Because of the pairing effect, only

[1] Some of masses of unstable nuclei, given in the tables of Audi (1992,1993), were actually semi-empirical evaluations based on the knowledge of masses of neighboring isotopes.

even-even nuclei are relevant for the ground state problem. For the remaining isotopes, up to the last one stable with respect to emission of a neutron pair, HP used theoretical masses obtained using a mass formula of Möller [59] (the description of the formalism can be found in Möller and Nix [60]).

The equilibrium nuclides present in the cold catalyzed matter are listed in Table 1. Only even-even nuclides are present, which results from additional binding due to nucleon pairing (see, e.g., [74]). In the fifth column of this table one finds the maximum density at which a given nuclide is present, $\rho_{\max}$. The value of the electron chemical potential, μ_e, at the density $\rho_{\max}$, is given in the sixth column. The transition to the next nuclide has a character of a first order phase transition and is accompanied by a density jump. The corresponding fractional increase of density, $\Delta\rho/\rho$, is shown in the last column of Table 1. The last row above the horizontal line, dividing the table into two parts, corresponds to the maximum density, at which the ground state of dense matter contains a nucleus observed in laboratory. The last line of Table 1 corresponds to the neutron drip point in the ground state of dense cold matter. This limiting density can be determined exclusively by the theoretical calculation.

Single-particle energy levels in nuclei are discrete, with large energy gaps between "major shells". The local maxima in the binding energies of nuclei with "magic numbers" $Z = 28$ and $N = 50,\ 82$ are associated with filling up these major shells (see, e.g., Preston and Bhaduri [74]). The effect of the closed proton and neutron shells on the composition of the ground state of matter is

Table 1. Nuclei in the ground state of cold dense matter. Upper part: experimental nuclear masses. Lower part: from mass mass formula of Möller [59]. Last line corresponds to the neutron drip point. After Haensel and Pichon [39].

element	Z	N	Z/A	$\rho_{\max}$ (g cm^{-3})	μ_e (MeV)	$\Delta\rho/\rho$ (%)
^{56}Fe	26	30	0.4643	$7.96\ 10^{6}$	0.95	2.9
^{62}Ni	28	34	0.4516	$2.71\ 10^{8}$	2.61	3.1
^{64}Ni	28	36	0.4375	$1.30\ 10^{9}$	4.31	3.1
^{66}Ni	28	38	0.4242	$1.48\ 10^{9}$	4.45	2.0
^{86}Kr	36	50	0.4186	$3.12\ 10^{9}$	5.66	3.3
^{84}Se	34	50	0.4048	$1.10\ 10^{10}$	8.49	3.6
^{82}Ge	32	50	0.3902	$2.80\ 10^{10}$	11.44	3.9
^{80}Zn	30	50	0.3750	$5.44\ 10^{10}$	14.08	4.3
^{78}Ni	28	50	0.3590	$9.64\ 10^{10}$	16.78	4.0
^{126}Ru	44	82	0.3492	$1.29\ 10^{11}$	18.34	3.0
^{124}Mo	42	82	0.3387	$1.88\ 10^{11}$	20.56	3.2
^{122}Zr	40	82	0.3279	$2.67\ 10^{11}$	22.86	3.4
^{120}Sr	38	82	0.3167	$3.79\ 10^{11}$	25.38	3.6
^{118}Kr	36	82	0.3051	($4.33\ 10^{11}$)	(26.19)	

very strong; except for the ^{56}Fe nucleus, present in the ground state at lowest densities, all nuclides are those with a closed proton or neutron shell (Table 1). A sequence of three increasingly neutron rich isotopes of nickel $Z = 28$ is followed by a sequence of $N = 50$ isotopes of decreasing Z, ending at the last experimentally identified ^{78}Ni. This last nuclid is doubly magic ($N = 50$, $Z = 28$).

At the densities 10^{11} g cm$^{-3} \lesssim \rho < \rho_{\rm ND}$ HP get a sequence of $N = 82$ isotopes, of decreasing proton number, from $Z = 44$ down to $Z = 36$, with neutron drip at $\rho_{\rm ND} = 4.3\ 10^{11}$ g cm^{-3} (Table 1). As shown by HP, results obtained using different mass formula, that of Pearson and collaborators (Pearson, 1993, private communication quoted in [39]) are quite similar to those obtained using the mass formula of Möller [59].

While the persistence of the $N = 50$ and/or $Z = 28$ nuclei in the ground state of the outer crust may be treated as an *experimental fact*, the strong effect of the $N = 82$, dominating at 10^{11} g cm$^{-3} \lesssim \rho < \rho_{\rm ND}$, might – in principle – be an artifact of the extrapolation via the semiempirical mass formulae. It should be mentioned, that some many-body calculations of the masses of very neutron rich nuclei suggest, that the effect of the closed $N = 82$ shell might be much weaker, and could be replaced by the strong effect of the closure of the $Z = 40$ subshell [36]. Clearly, there is a need for better understanding of shell effects in nuclei close to the neutron drip.

4 Ground state of the matter in the inner crust for $\rho \lesssim 10^{14}$ g cm^{-3}

The existence of the inner neutron-star crust, in which very neutron rich nuclei are immersed in a gas of dripped neutrons, has been realized long before the discovery of pulsars (in 1958, [41]). First approach to describe this layer of neutron star envelope consisted in employing a semiempirical mass formula to calculate (or rather estimate) the masses of nuclei, combined with an expression for the energy of neutron gas [41],[42],[88], [51],[6]. It is worth to be mentioned that as early as in 1965 neutron drip density and the density at the bottom edge of the inner crust were estimated as $\rho_{\rm ND} \simeq 3 \times 10^{11}$ g cm^{-3} and $\rho_{\rm edge} \simeq 8 \times 10^{13}$ g cm^{-3} [88], surprisingly close to the presently accepted values of these densities. Further work concentrated on a consistent (unified) description of nuclear matter inside neutron rich nuclei, and of neutron gas outside them, using a single expression for the energy density of nuclear matter as a function of neutron and proton densities and of their gradients [3],[18],[19], [1]. The most ambitious early attempt to calculate the ground state of the inner crust was the Hartree-Fock calculation of Negele and Vautherin [62]. Later work focused on the consistent description of the bottom layers of the crust and included up-dated treatment of both pure neutron matter and effective nucleon-nucleon interaction [43],[66],[67],[55], [87],[28],[31],[30].

In general, calculations of the structure, composition, and equation of state of the inner crust can be divided into three groups, according to the many-body

technique used. Full quantum mechanical treatment can be carried out within the Hartree-Fock approximation with an effective nucleon-nucleon interaction. Further approximation of the many-body wave function can be done using semi-classical Extended Thomas-Fermi (ETF) approximation. Basic quantities within the ETF are neutron and proton densities and their spatial gradients. Finally, investigations belonging to the third group use Compressible Liquid Drop Model (CLDM) parameterization for the description of nuclei, with parameters derived within a microscopic nuclear many-body theory (HF or ETF) based on an effective nucleon-nucleon interaction.

4.1 Hartree-Fock calculations with effective nucleon-nucleon interaction

Matter is divided into unit cells, which are electrically neutral and contain one nucleus, with cell volume $V_{\rm c} = 1/n_{\mathcal{N}}$. Let us assume that a unit cell contains N neutrons and Z protons. The nuclear effective hamiltonian for such a system of $A = N + Z$ nucleons is

$$H_{\rm N}^{\rm eff} = \sum_{j=1}^{A} t_j + \frac{1}{2} \sum_{j,k=1, j\neq k}^{A} v_{jk}^{\rm eff} \ , \tag{5}$$

where t_j is the kinetic energy operator of j-th nucleon, while $v_{jk}^{\rm eff}$ is an operator of effective two-body interaction between the jk nucleon pair. Usually, $v_{jk}^{\rm eff}$ contains a component which is an effective two-body representation of the three-body forces, important in dense nucleon medium.

Effective nuclear hamiltonian $H_{\rm N}^{\rm eff}$ has to reproduce - as well as possible, and within the Hartree-Fock approximation - relevant properties of the ground state of the many-nucleon system, and in particular - ground state energy, E_0. This last condition can be written as $\langle \Phi_0 | H_{\rm N}^{\rm eff} | \Phi_0 \rangle \simeq \langle \Psi_0 | H_{\rm N} | \Psi_0 \rangle$, where Φ_0, Ψ_0, and $H_{\rm N}$ are Hartree- Fock wave function, real wave function, and real nuclear Hamiltonian, respectively.

The complete hamiltonian of a unit cell is $H_{\rm cell}^{\rm eff} = H_{\rm N}^{\rm eff} + V_{\rm Coul} + H_e$, where $V_{\rm coul}$ and H_e are the components corresponding to Coulomb interaction between charged constituents of matter (protons and electrons), and that of a uniform electron gas, respectively. The Hartree-Fock approximation for the many-body nucleon wave function is

$$\Phi_{NZ} = \mathcal{C}_{NZ} \ \det \left[\varphi_{\alpha_i}^{(p)}(\xi_k) \right] \det \left[\varphi_{\beta_j}^{(n)}(\zeta_l) \right] \ , \tag{6}$$

where $\varphi_{\beta_j}^{(n)}(\zeta_l)$ and $\varphi_{\alpha_i}^{(p)}(\xi_k)$ are single-particle wave functions (orbitals) for neutrons $(j, l = 1, ..., N)$ and protons $(i, k = 1, ..., Z)$, respectively, and $\mathcal{C}_{NZ}$ is normalization constant. The space and spin coordinates of k-th proton and j-th neutron are represented by ξ_k and ζ_l, while $\{\alpha_i\}$ and $\{\beta_j\}$ are sets of quantum numbers of occupied single-particle states for protons and neutrons, respectively.

Further approximation, used by Negele and Vautherin [62], consisted in imposing the spherical symmetry. Unit cell was approximated by a sphere, and quantum numbers of single-particle states were therefore nlj. The Hartree-Fock equations for $\varphi^{(p)}$ and $\varphi^{(n)}$ were derived from the minimization of the HF energy functional, at fixed volume of the unit cell, $V_{\rm c}$,

$$E_{\rm cell}\left[\varphi_\alpha^{(p)},\varphi_\beta^{(n)}\right] = \langle \Phi_{NZ}\Phi_e \left| H_{\rm cell}^{\rm eff}\right| \Phi_{NZ}\Phi_e\rangle = \text{minimum}\ , \tag{7}$$

where Φ_e is the plane-wave Slater determinant for the ultrarelativistic electron gas of constant density $n_e = Z/V_{\rm c}$. Minimization, performed at fixed $V_{\rm c}$, corresponds to fixed average neutron and proton densities, $n_n = N/V_{\rm c}$, $n_p = Z/V_{\rm c} = n_{\mathcal{N}}Z$. For details concerning actual calculational procedure the reader is referred to the original paper of Negele and Vautherin [62].

Having calculated the HF orbitals, $\varphi_\beta^{(n)}$, $\varphi_\alpha^{(p)}$, one determines the minimum (ground state) value of $E_{\rm cell}(N,Z)$, filling lowest N neutron states and Z proton states. Then, the absolute ground state configuration is found by minimizing $E_{\rm cell}(N,Z)$ at fixed $A = N + Z$. Let us notice, that α_Z and β_N correspond then to the "Fermi level" for protons and neutrons, respectively. In terms of the single-nucleon orbitals, the neutron drip point corresponds to the threshold density, at which neutron Fermi level becomes *unbound*, i.e., $\phi_{\beta_N}^{(n)}$ extends over the whole unit cell. Even at highest densities considered, no proton drip occurs. As the matter density increases, the neutron gas density outside nuclei increases, and the density of protons within nuclei decreases. As Negele and Vautherin [62] find, at $\rho \gtrsim 8\times 10^{13}$ g cm^{-3} the differences in energy between various local minima of $E_{\rm cell}(N,Z)$ become so small, that it is not meaningful to proceed with their calculational scheme to higher density.

One of the most interesting results of Negele and Vautherin [62] was prediction of strong shell effect for protons: it is visualized by persistence of $Z = 40$ (closed proton subshell) from neutron drip point to about 3×10^{12} g cm^{-3}, and $Z = 50$ (closed major proton shell) for 3×10^{12} g cm$^{-3} \lesssim \rho \lesssim 3\times 10^{13}$ g cm^{-3}, Fig.2.

Alas, apart from the work of Negele and Vautherin [62], no other attempt of a Hartree-Fock calculation of nuclear structures in the ground state of the inner crust was carried out. This might result from an unsolved problem of correct treatment of the boundary conditions at the unit cell edge, accompanied by difficulties in finding absolute minimum of the Hartree-Fock energy functional. These problems did not prevent carrying-out Hartree-Fock unit-cell calculations of nuclear structures in hot dense matter, relevant for the equation of state in the gravitational collapse of stellar cores [14], [91]. This seems to be due to the fact that thermal averaging at $k_{\rm B}T \gtrsim 1$ MeV, as well as much less important role of the nucleon gas outside nuclei, in the relevant case of entropy per nucleon $\sim 1-2\ k_{\rm B}$, makes the calculation less dependent on a somewhat arbitrary choice of the boundary condition at the unit cell edge.

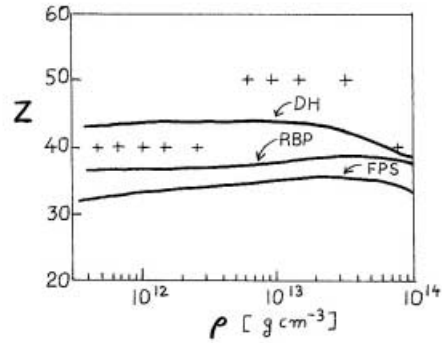

Fig. 2. Numbers of protons per nucleus in the ground state of the inner crust, obtained by various authors. Solid lines: RBP - Ravenhall et al. [76]; FPS - as quoted in [72]; DH - Douchin and Haensel [30]. Crosses - Negele and Vautherin [62].

4.2 Extended Thomas-Fermi calculations

Above neutron drip, the number of nucleons in the unit cell grows rapidly with increasing density. At $\sim 10^{13}$ g cm^{-3} one has $A_{\rm cell} \sim 1000$ [62], and implementation of the self-consistent HF scheme requires an enormous amount of work and computer time. Large size of nuclei suggests further simplifications of the HF model via *semiclassical approximation*, in which relevant quantities are represented "on the average", with quantum fluctuations (oscillations) being averaged out. The energy of a unit cell is a sum of a nuclear energy $E_{\rm N}$ (which includes nucleon rest energies), Coulomb energy $E_{\rm coul}$, and energy of electron gas, E_e. In the Extended TF approximation (see, e.g., [79],[16]), nuclear energy of a unit cell is expressed in terms of energy density functional $\mathcal{E}_{\rm N}$ as

$$E_{\rm N} = \int_{\rm cell} \{\mathcal{E}_{\rm N}\left[n_n(\mathbf{r}), n_p(\mathbf{r}), \nabla n_n(\mathbf{r}), \nabla n_p(\mathbf{r})\right]\} \, {\rm d}^3 r$$
$$+ \int_{\rm cell} \left[m_n c^2 n_n(\mathbf{r}) + m_p c^2 n_p(\mathbf{r})\right] {\rm d}^3 r \ . \tag{8}$$

The nuclear energy density functional has a non-local character, as it depends on the density gradients. For the ETF approximation to be valid, characteristic length over which density n_n or n_p changes significantly has to be much larger than the mean internucleon distance. One can then restrict to keeping only quadratic gradient terms in $\mathcal{E}_{\rm N}$. To a very good approximation, electron gas is uniform, with $n_e = Z/V_{\rm c}$, and therefore Coulomb energy of a unit cell is given by

$$E_{\rm Coul} = \frac{1}{2} \int_{\rm cell} e\left[n_p(\mathbf{r}) - n_e\right] \phi(\mathbf{r}) {\rm d}^3 r \ , \tag{9}$$

where $\phi(\mathbf{r})$ is the electrostatic potential, to be calculated from the Poisons equation,

$$\nabla^2 \phi(\mathbf{r}) = -4\pi e \left[n_p(\mathbf{r}) - n_e\right] \ , \tag{10}$$

and e is the elementary charge. To calculate the ground state at a given n_b, one has to find $n_n(\mathbf{r})$, $n_p(\mathbf{r})$, which minimize $E_{\rm cell}/V_{\rm c}$, under the constraints

$$V_{\rm c} n_b = \int_{\rm cell} [n_n(\mathbf{r}) + n_p(\mathbf{r})]\, {\rm d}^3 r \ , \qquad \int_{\rm cell} [n_p(\mathbf{r}) - n_e]\, {\rm d}^3 r = 0 \ . \tag{11}$$

The unit cell is approximated by a sphere of radius $r_{\rm c} = (3V_{\rm c}/4\pi)^{1/3}$, which simplifies the problem due to spherical symmetry. The boundary conditions are such that far from the nuclear surface (i.e., from the neutron gas–nuclear matter interface) nucleon densities are uniform. This requires that nuclear radius be significantly smaller than $r_{\rm c}$. The ETF method was first applied to the calculation of the structure of the inner crust by Buchler and Barkat ([18], see also [19] and [2]). In the 1980s the main effort was concentrated on the case of dense and hot matter, relevant for the gravitational collapse of stellar cores and for modeling of type II supernova explosions An exception from this rule is the paper of Ogasawara and Sato [63], who devote Sect.3.1 of their paper to the case of cold catalyzed matter. Their calculational scheme was similar to that used by Barkat et al. [2]. However, Ogasawara and Sato used different models of potential energy of asymmetric nuclear matter. They obtained neutron drip density $3 - 4 \times 10^{11}$ g cm^{-3} and the values of $Z = 35 - 45$, higher than those of [2]; this difference resulted from different nuclear energy functional models. Results of Ogasawara and Sato were in good agreement with HF results of Negele and Vautherin [62].

Significant progress in the 1980s was achieved in the calculations of the properties of asymmetric nuclear matter and pure neutron matter with realistic bare nucleon-nucleon interactions (see, [33],[90]). On the other hand, calculations using the HF method and its semi-classical simplifications, with new models of effective nucleon-nucleon interaction, reached a high degree of precision in reproducing the properties of atomic nuclei. The ETF calculation in the 1990s focused on detailed investigation of the possibility of appearance of non-spherical nuclei in the densest layer of the crust, which will be described in detail in Sect.5. Oyamatsu [67] studied the ground state of the inner crust within the ETF approximation, with four different energy density functionals $\mathcal{E}_{\rm N}$. These functionals were constructed so as to reproduce gross properties of laboratory nuclei, and to be consistent with the equation of state of pure neutron matter obtained by Friedman and Pandharipande [33] for realistic bare nucleon-nucleon interaction. Oyamatsu performed explicit minimization of the TF energy functional within a family of *parameterized* n_n and n_p density profiles. Between neutron drip, which takes place at 4×10^{11} g cm^{-3}, and 10^{14} g cm^{-3}, Oyamatsu obtained for all four of his models $Z \simeq 40$, in good agreement with HF calculations of Negele and Vautherin [62].

Simultaneously with application of the relativistic Brueckner-Hartree-Fock (RBHF) approach to neutron star matter at supranuclear densities, semi-classical ETF approximation based on the RBHF model was applied for the calculation of the properties of the inner crust. Starting from the RBHF results for bulk asymmetric nuclear matter, Sumiyoshi et al. [87] applied the ETF

scheme of Oyamatsu [67], with his parameterization of the nucleon density profiles. The quadratic gradient term in the energy density functional was determined by fitting the properties of terrestrial nuclei. They found neutron drip at 2.4×10^{11} g cm^{-3}. Their values of Z in the inner crust were systematically lower than those obtained in older work, with $Z \simeq 35$ near neutron drip, decreasing down to about 20 at $\rho \simeq 10^{14}$ g cm^{-3}. This may be attributed to the fact that Coulomb energy of nuclei in their model is relatively large, due to smaller nuclear radii. It should be mentioned that their RBHF value of saturation density for symmetric nuclear matter, 0.185 fm^{-3}, was significantly larger than the experimental value of 0.16 fm^{-3} and this may explain compactness of their nuclei.

Relativistic Hartree approximation of the ground-state energy functional, calculated in the non-linear relativistic mean field model of dense nucleon matter, can be simplified using the relativistic extended Thomas-Fermi (RETF) approximation proposed by Centelles et al. [24],[25]. In the RETF approximation, one gets $\mathcal{E}_{\rm N}$ functional containing terms quadratic in ∇n_n, ∇n_p, which are completely determined within the model. The RETF model was applied by Cheng et al. [28] for the calculations of the structure of the ground state of the inner crust, starting from the Boguta and Bodmer [13] nonlinear $\sigma - \omega - \rho$ model Lagrangian. Three sets of the Lagrangian parameters were used in actual calculations. Cheng et al. [28] solved the Euler-Lagrange equations for $n_n(r)$, $n_p(r)$ in the spherical unit cell exactly. They did not give explicitly values of Z as function of the matter density. However, analysis of their figures and tables leads to conclusion that, similarly as Sumiyoshi et al. [87], they get nuclei which are relatively small, and their values of Z are significantly lower than those obtained in non-relativistic calculations.

4.3 Compressible liquid drop model

The nature of the HF and ETF calculations does not permit to study separate physical contributions and effects, whose interplay leads to a particular structure of the inner crust. The compressible liquid drop model (CLDM) enables one to separate various terms in $E_{\rm cell}$, so that their role and mutual interaction can be identified.

There are also practical advantages of using the CLDM. On the one hand, it can be considered as suitable and economical parameterization of results of microscopic calculations of the HF or ETF type. On the other hand, CLDM model avoids technical complications related to the choice of boundary conditions at the edge of the unit cell, plaguing HF approach at highest inner crust densities. Finally, CLDM description allows for thermodynamically consistent and systematic treatment of bulk and finite-size effects, and is particularly convenient for studying phase transitions between different phases of neutron star matter (see Sect.5). In particular, CLDM treats two major effects of the outer neutron gas on nuclei: 1) decrease of the surface tension with growing density, due to increasing similarity of nucleon matter inside and outside nuclei; 2) compression of nuclear matter within nuclei due to the pressure of outer neutron gas.

However, we should stress that all these attractive features of the CLDM model are valid only when finite-size contributions were calculated, in a microscopic HF or ETF approach, from the same effective nucleon hamiltonian as that used for the calculation of the bulk (volume) terms. In particular, only in such a case decrease of the surface tension due to the presence of the outer neutron gas is treated in a correct way.

Within the CLDM, one divides nuclear contribution $E_{\rm N}$ (which excludes Coulomb interactions) to $E_{\rm cell}$ into bulk, $E_{\rm N,bulk}$ and surface, $E_{\rm N,surf}$, terms. Coulomb contributions to the energy of a unit cell are denoted by $E_{\rm Coul}$. Electrons are assumed to form an uniform Fermi gas, and yield the rest and kinetic energy contribution, denoted by E_e. Total energy of a unit cell is therefore given by

$$E_{\rm cell} = E_{\rm N,bulk} + E_{\rm N,surf} + E_{\rm Coul} + E_e \ . \tag{12}$$

Here, $E_{\rm N,bulk}$ is the bulk contribution of nucleons, which does not depend on the size and shape of nuclear structures. However, both $E_{\rm N,surf}$ and $E_{\rm Coul}$, which vanish for uniform *npe* matter, do depend on the size and shape of nuclear structures, formed by denser nuclear matter and the less dense neutron gas. From the point of view of thermodynamics, nucleons are distributed between

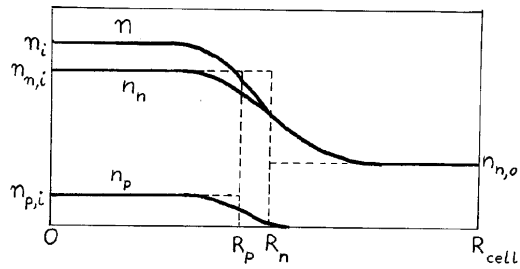

Fig. 3. Proton and neutron number density distributions within a spherical unit cell in the inner neutron star crust. Solid lines are actual density profiles, dashed lines correspond to those of the Compressible Liquid Drop Model. R_n, R_p are equivalent neutron and proton radii, denoted in the text as r_n, r_p.

three subsystems: denser nucleon fluid, which will be labeled by "i", less dense neutron fluid, labeled by "o", and nuclear surface (i.e., "i-o" phase interface), labeled by "s". One requires mechanical and chemical equilibrium between these subsystems. Far from the nuclear surface, nucleon densities are constant, and equal to $n_{n,\rm i}$, $n_{p,\rm i}$ in the denser "i" phase and $n_{n,\rm o}$ in the less dense neutron gas. The definition of the surface term is subject to an ambiguity. In the case of spherical nuclei in the inner crust it is convenient to identify it with a sphere of *reference proton radius* r_p, such that $\frac{4\pi}{3} r_p^3 n_{p,\rm i}$ is equal to the actual Z. Such a definition is convenient because of the presence of the Coulomb term in $E_{\rm cell}$,

which involves solely proton density distribution. Similarly, neutron radius r_n is defined by $\frac{4\pi}{3}[r_n^3(n_{n,\mathrm{i}}-n_{n,\mathrm{o}})+r_\mathrm{c}^3 n_{n,\mathrm{o}}] = N_\mathrm{cell}$ (see Fig.3). In view of a significant neutron excess, the interface includes *neutron skin*, of thickness $s_n = r_n - r_p$, formed by neutrons adsorbed onto the nuclear matter surface.

The nuclear bulk energy of a cell is

$$E_{\mathrm{N,bulk}} = V_\mathrm{c}\left[w\mathcal{E}_{\mathrm{N,i}} + (1-w)\mathcal{E}_{n,\mathrm{o}}\right] \ , \tag{13}$$

where the volume of the cell $V_\mathrm{c} = 4\pi r_p^3/3$, $\mathcal{E}_{\mathrm{N,i}}$ is energy density of nuclear matter far from nuclear surface, and $\mathcal{E}_{n,\mathrm{o}}$ is the corresponding quantity for outer neutron gas. The volume fraction occupied by the phase "i" is $w = V_p/V_\mathrm{c} = (r_p/r_\mathrm{c})^3$.

The nuclear surface energy term, $E_{\mathrm{N,surf}}$, gives the contribution of the interface between neutron gas and nuclear matter; it includes contribution of neutron skin ([52],[72],[54]),

$$E_{\mathrm{N,surf}} = \mathcal{A}\sigma + N_\mathrm{s}\mu_{n,\mathrm{s}} \ , \tag{14}$$

where σ is the *surface thermodynamic potential per unit area*, $\mathcal{A}$ is the area of nuclear surface (in the case of spherical nuclei $\mathcal{A} = 4\pi r_p^2$), N_s is the number of neutrons in neutron skin, and $\mu_{n,\mathrm{s}}$ is the chemical potential of the neutrons adsorbed onto reference proton surface. In the simplest approximation, in which curvature contributions to $E_{\mathrm{N,surf}}$, proportional to $\mathcal{A}/r_p$, are neglected, σ is approximated by the *surface tension* σ_s, and $N_\mathrm{s} \simeq (n_{n,\mathrm{i}} - n_{n,\mathrm{o}})s_n\mathcal{A}$. More precise expression for $E_{\mathrm{N,surf}}$ may be obtained including curvature corrections, which take into account the curvature of the nuclear surface ([54],[29]). In view of the possibility of nuclear structures with infinite volumes (see Sect.5) it is convenient to introduce contribution of neutrons in neutron skin to the total (overall) nucleon density, $n_\mathrm{s} = N_\mathrm{s}/V_\mathrm{c}$ [54].

In order to calculate E_Coul, one uses the Winger-Seine approximation. Neglecting diffuseness of the proton distribution one gets

$$E_\mathrm{Coul} = \frac{16}{15}\pi^2\left(n_{p,\mathrm{i}}e\right)^2 r_p^5 f_3(w) \ , \qquad f_3(w) = \left(1 - \frac{3}{2}w^{1/3} + \frac{1}{2}w\right) \ . \tag{15}$$

At $T = 0$, equilibrium can be determined by minimizing total energy density, $\mathcal{E} = E_\mathrm{cell}/V_\mathrm{c}$, at fixed value of n_b. The quantity $\mathcal{E}$ is a function of seven independent variables. A convenient set of variables is: $n_{n,\mathrm{i}}$, $n_{p,\mathrm{i}}$, n_s, $n_{n,\mathrm{o}}$, r_p, r_n, r_c; in this way all independent variables will be finite even in the case of infinite nuclear structures, considered in Sect. 5. Imposing fixed n_b, and requiring charge neutrality of the cell, we reduce the number of independent variables to five. Therefore, there will be five conditions of equilibrium resulting from the stationarity of $\mathcal{E}$ with respect to variations of thermodynamic variables. Each of these conditions has well defined physical meaning. First condition requires that the neutron chemical potential in the nucleus and in the outer neutron gas be the same. Neglecting curvature corrections, it implies equality of neutron chemical potentials in the bulk phases of nucleon matter, $\mu_{n,\mathrm{i}}^{\mathrm{bulk}} = \mu_{n,\mathrm{o}}^{\mathrm{bulk}}$. Second equation results from minimization with respect to the number of protons, and yields the beta equilibrium condition between neutrons, protons, and electrons. Neglecting

curvature corrections, it reads

$$\mu_{n,\mathrm{i}}^{\mathrm{bulk}} - \mu_{p,\mathrm{i}}^{\mathrm{bulk}} - \mu_e = \frac{8\pi}{5} e^2 n_{p,\mathrm{i}} r_p^2 f_3(w) \ . \tag{16}$$

We also need a condition on the number of surface neutrons. It results from the requirement of stationarity with respect to transfer of a neutron from the nucleus interior to the surface, all other particle numbers being fixed. Neglecting curvature corrections, this condition implies that the chemical potential of surface neutrons is equal to the bulk chemical potentials in both phases, $\mu_{n,\mathrm{s}} = \mu_{n,\mathrm{i}}^{\mathrm{bulk}} = \mu_{n,\mathrm{o}}^{\mathrm{bulk}}$.

To these three conditions, expressing chemical equilibrium within the system, we have to add two equations corresponding to mechanical equilibrium. Condition number four results from the requirement of stationarity with respect to change of r_p, and expresses the equalities of pressures inside and outside the nucleus. Neglecting curvature corrections, condition number four reads

$$P_{\mathrm{i}}^{\mathrm{bulk}} - P_{\mathrm{o}}^{\mathrm{bulk}} = \frac{2\sigma_{\mathrm{s}}}{r_p} - \frac{4\pi}{15} e^2 n_{p,\mathrm{i}}^2 r_p^2 (1-w) \ , \tag{17}$$

where $P_{\mathrm{j}}^{\mathrm{bulk}} = n_{\mathrm{j}}^2 \partial(\mathcal{E}_{\mathrm{j}}^{\mathrm{bulk}}/n_{\mathrm{j}})/\partial n_{\mathrm{j}}$.

The last fifth equation determines the equilibrium size of the cell. It results from the condition of stationarity with respect to the variation spatial scale of the cell, while w and all densities including n_{s} are kept constant. Notice, that because w is kept constant, this condition involves only the finite-size terms in E_{cell}. Within our approximation (no curvature corrections), the last condition can be written as

$$E_{\mathrm{N,surf}} = 2E_{\mathrm{Coul}} \ . \tag{18}$$

This the "virial theorem" of the simplified Compressible Liquid Drop Model with no curvature corrections (Baym, Bethe, and Pethick [3], hereafter referred to as BBP), which enables one to express r_p in terms of remaining variables. Generalization of "virial theorem" to the case of nonstandard nuclear shapes will be discussed in Sect.5.

Let us write an explicit expression for nuclear component of the energy density, neglecting for simplicity curvature corrections in $E_{\mathrm{N,surf}}$. Both surface tension, $\sigma \simeq \sigma_{\mathrm{s}}$, and thickness of neutron skin, $s_n = r_n - r_p$, are calculated under the condition of thermodynamic and mechanical equilibrium of the semi-infinite "i" and "o" phases, separated by a plane interface. Therefore, σ and s_n depend on only one thermodynamic variable, e.g., proton fraction in the bulk "i" phase, $x_{\mathrm{i}} = n_{p,\mathrm{i}}/n_{\mathrm{i}}$, where $n_{\mathrm{i}} = n_{n,\mathrm{i}} + n_{p,\mathrm{i}}$. The formula for the energy density $\mathcal{E}_{\mathrm{N}}$ reads then

$$\mathcal{E}_{\mathrm{N}} = w\mathcal{E}_{\mathrm{N,i}} + (1-w)\,\mathcal{E}_{n,\mathrm{o}} + \frac{3w}{r_p}\left[\sigma_{\mathrm{s}} + (n_{n,\mathrm{i}} - n_{n,\mathrm{o}}) s_n \mu_n\right] \ . \tag{19}$$

Let us remind, that in equilibrium chemical potential of neutrons adsorbed onto nuclear surface is equal to the common value of μ_n in both bulk phases. Possibility of non-spherical shapes of nuclei will be considered in the next Section.

Historically, first CLDM calculations of the structure of the inner crust were performed in the classical paper of Baym, Bethe, and Pethick [3](BBP). The BBP paper formulated the foundations of the subsequent CLDM calculations of the structure of the inner neutron star crust. Unfortunately, BBP used oversimplified estimates of the reduction of σ with increasing density, based on dimensional arguments; this resulted in rapid increase of Z with increasing density, corrected in subsequent calculations [76]. Most recent CLDM calculation of the ground state structure of the inner crust were performed by Lorenz [54] and by Douchin and Haensel ([29], [31],[30]). These calculations were based of effective nucleon-nucleon interactions, which were particularly suitable for strongly asymmetric nuclear systems. Lorenz used FPS model (**F**riedman **P**andharipande **S**kyrme [70]), consistent with results of many-body calculations of dense asymmetric nuclear matter with realistic bare nucleon-nucleon interaction and a phenomenological three-nucleon force, performed by Friedman and Pandharipande [33]. Douchin and Haensel used the SLy (**S**kyrme **Ly**on, [26],[27]) effective forces, adjusted to the properties of neutron-rich nuclei, and adjusted also, at $\rho > \rho_0$, to the results of many-body dense asymmetric nuclear matter calculations of Wiringa et al. [90], which were based on bare two-nucleon interaction AV14 and phenomenological UVII three-nucleon interaction.

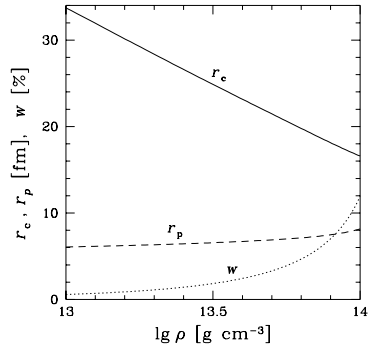

Fig. 4. Radius of spherical unit (Winger-Seine) cell, r_c, the proton radius of spherical nuclei, r_p, and fraction of volume filled by protons, w (in percent), versus matter density ρ. Based on Douchin and Haensel [30].

In what follows, we will illustrate CLDM results for spherical nuclei by those of Douchin and Haensel [30]. Geometrical parameters characterizing nuclei in the inner crust, up to 10^{14} g cm^{-3}, are shown in Fig. 4. Here, w is the fraction of volume occupied by nuclear matter (with our definition of nuclear matter volume equal to that occupied by protons).

More detailed information on neutron-rich nuclei, present in the ground state of the inner crust at $\rho < 10^{14}$ g cm^{-3}, can be found in Fig.5. Number of nucleons in a nucleus, A, grows monotonically, and reaches about 300 at 10^{14} g cm^{-3}, where $A_{\rm cell} \simeq 1000$. However, the number of protons changes rather weakly,

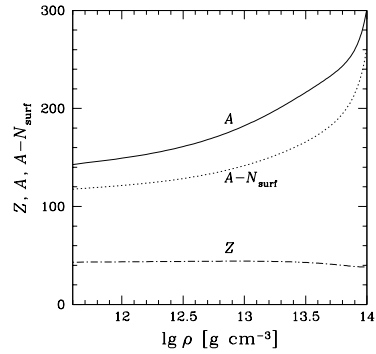

Fig. 5. Mass number of spherical nuclei, A, and their proton number, Z, versus average matter density ρ. Dotted line corresponds to number of nucleons after deducing neutrons belonging to neutron skin ($N_{\rm surf}$ corresponds to $N_{\rm s}$ in the text). Based on Douchin and Haensel [30].

increasing slightly from $Z \simeq 40$ near neutron drip to somewhat above forty at 10^{13} g cm^{-3}, and then decreasing to $Z \simeq 40$ at 10^{14} g cm^{-3}. Results for Z of spherical nuclei are quite similar to those obtained in ([67],[76]), but are somewhat higher than those obtained using a relativistic mean-field model in ([87],[28]). An interesting quantity is the number of neutrons forming neutron skin, $N_{\rm s}$. As one can see from Fig.5, for $\rho \gtrsim \frac{1}{3}\rho_0$ the value of $N_{\rm s}$ decreases with increasing density; this is due to the fact that $n_{n,{\rm i}}$ and $n_{n,{\rm o}}$ become more and more alike.

For $\rho \simeq 10^{14}$ g cm^{-3}, spherical nuclei are very heavy, $A \simeq 300$, and doubts concerning their stability with respect to deformation and fission arise.

Originally, the Bohr-Wheeler condition for fission has been derived for isolated nuclei, which were treated as drops of incompressible, charged nuclear matter (see, e.g., [74]). Let us denote the Coulomb and surface energy of a spherical nucleus *in vacuum* by $E^{(0)}_{\rm Coul}$ and $E^{(0)}_{\rm surf}$, respectively. The Bohr-Wheeler conditions states that for $E^{(0)}_{\rm Coul} \geq 2E^{(0)}_{\rm surf}$ a spherical nucleus is unstable with respect to small quadrupolar deformations, and is therefore expected to deform spontaneously and fission into smaller drops (fragments). In the case of nuclei in the neutron-star crust one has to include corrections to the Bohr-Wheeler condition, resulting from the presence of electron background and of other nuclei. Such corrections were calculated by Brandt (1985; quoted in [72]). The leading corrections were found to be of the order of $(r_p/r_{\rm c})^3$. This is to be contrasted with corrections in $E_{\rm Coul}$, where the leading correction term is linear in $r_p/r_{\rm c}$ [see (15)]. Keeping only leading correction to Coulomb energy, one can rewrite the equilibrium condition, (18), in an approximate form

$$E_{\rm surf} \simeq 2E^{(0)}_{\rm Coul}\left(1 - \frac{3}{2}\frac{r_p}{r_{\rm c}}\right) \ . \tag{20}$$

Within the linear approximation, $E^{(0)}_{\rm Coul}$ is the Coulomb energy of the the nucleus itself (self-energy). The quantity $E^{(0)}_{\rm Coul}$ is larger than the actual $E_{\rm Coul}$, which is equal to the half of $E_{\rm surf}$. As the density increases, $E^{(0)}_{\rm Coul}$ can become sufficiently large for the Bohr-Wheeler condition to be satisfied. Within linear approximation, this would happen for $r_p/r_{\rm c} > 1/2$, i.e., when nuclei fill more than $(1/2)^3 = 1/8$ of space. As one sees from Fig.4, this does not happen for spherical nuclei at $\rho < 10^{14}$ g cm^{-3} for the particular Douchin and Haensel [30] model of the inner crust. However, at 10^{14} g cm^{-3} the value of $w = (r_p/r_{\rm c})^3$ is rather close to the critical value of 1/8.

5 Ground state of the matter in the bottom layers of the crust

For $\rho \lesssim 10^{14}$ g cm^{-3} ground state of the inner crust contains spherical nuclei; as we will see in the present section, such a structure is stable with respect to transition into different nuclear shapes, or into a uniform *npe* matter. Of course, as long as $r_p \ll r_{\rm c}$, we *expect* nuclei in the ground state of dense cold matter to be spherical (or quasispherical). This is particularly clear within the CLDM, where for $r_p \ll r_{\rm c}$ it is the spherical shape which minimizes the shape-dependent (finite-size) contribution $E_{\rm N,surf} + E_{\rm Coul}$. However, the situation at $\rho \gtrsim 10^{14}$ g cm^{-3}, where $r_p/r_{\rm c} \gtrsim 0.5$, is far from being obvious.

In the present section we will study, in the ground state approximation, the structure and equation of state of the inner crust at $\rho \gtrsim 10^{14}$ g cm^{-3}. In particular, we will discuss possible unusual (exotic) shapes of nuclei present in the bottom layers of the crust. We will also study transition between the crust and the liquid neutron star core.

5.1 Unusual nuclear shapes

Long ago it has been pointed out that when the fraction of volume occupied by nuclear matter exceeds 50%, nuclei will turn "inside-out", and spherical bubbles of neutron gas in nuclear matter will become energetically preferred (BBP). [2] Generally, in the process of minimization of energy, nuclear shape has to be treated as a thermodynamic variable: the actual shape of nuclei in the ground state of the bottom layer of the inner crust has to correspond to the minimum of $\mathcal{E}$ at a given n_b. Historically, first studies along these lines were connected with structure of matter in gravitational collapse of massive stellar cores. Calculations performed within the CLDM for dense hot matter, with $T > 10^{10}$ K and entropy per nucleon $1 - 2\ k_{\rm B}$ indicated, that before the transition into uniform plasma, matter undergoes a series of phase transitions, accompanied by a change of nuclear shape [77]. These authors considered a basic set of spherical, cylindrical, and planar geometries, corresponding to *dimensionality* $d = 3,\ 2,\ 1$. For

[2] This result of BBP was obtained within the Liquid Drop Model, neglecting curvature contribution to the surface thermodynamical potential.

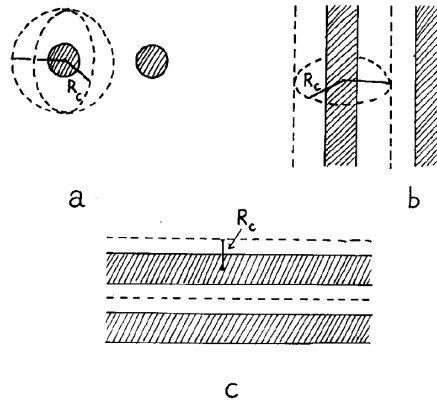

Fig. 6. Unit cells for a set of nuclear shapes (spheres, rods, plates) in the inner crust. The radius of the unit cell is denoted by $R_{\rm c}$ (notation in the text: $r_{\rm c}$). Hatched regions correspond to nuclear matter, blank to neutron gas. In the case of the "bubbular phase" (tubes, spherical bubbles) one has to exchange the roles of the blank and hatched regions.

each dimensionality, they restricted to simplest shapes with a single curvature radius (i.e., maximal symmetry). So, for $d = 3$ Ravenhall et al. [77] considered spherical nuclei in nucleon gas and spherical bubbles in denser nuclear matter, referred to as 3N and 3B, respectively. In the case of $d = 2$, nuclear structures were cylindrical nuclei (rods, 2N), and cylindrical holes in nuclear matter, filled with nucleon gas (tubes, 2B). Finally, for $d = 1$ they considered parallel plates of nuclear matter separated by nucleon gas; in this case "bubbular" and "nuclear" phases coincide, and were denoted by 1N. [3] Ravenhall et al. [77] found a sequence of phase transitions 3N $\longrightarrow$ 2N $\longrightarrow$ 1N $\longrightarrow$ 2B $\longrightarrow$ 3B, which preceded transition into uniform plasma. These transitions were accompanied by increase of the fraction of volume occupied by denser (nuclear matter) phase.

One of the virtues of the CLDM is its flexibility as far as the shape of nuclei is concerned. The terms $\mathcal{E}_{\rm N,bulk}$ and $\mathcal{E}_e$ are shape independent. The surface and Coulomb terms do depend on the shape of nuclei, but can easily be calculated if one neglects the curvature corrections. In what follows we will describe the formulae for $\mathcal{E}_{\rm N,surf}$ and $\mathcal{E}_{\rm Coul}$ within this simple approximation. For the sake of completeness, we will include also previously considered case of spherical nuclei (phase 3N). Using elementary considerations, one may show that the general formula for the surface energy contribution is

$$\mathcal{E}_{\rm N,surf} = \frac{wd}{r_p}\left[(n_{n,{\rm i}} - n_{n,{\rm o}})\,\mu_n s_n + \sigma_{\rm s}\right] \ , \tag{21}$$

[3] For obvious reasons, culinary terms are also frequently used to denote various phases. So, 3B, 2N, and 1N are referred to as *swiss cheese*, *spaghetti*, and *lasagna* phases, respectively.

where dimensionality the $d = 3$ for 3N, 3B phases, $d = 2$ for the 2N, 2B phases, and $d = 1$ for the 1N phase. The filling factor w is given by a simple formula $w = (r_p/r_c)^d$.

The case of the Coulomb contribution is more complicated, but the result can be also represented by a universal expression, obtained in [77]. The calculation is based on the Winger-Seine approximation. The unit cells for the 3N, 2N and 1N phases are visualized in Fig. 6. In the case of rods, the unit cell is approximated by a cylinder, coaxial with the rod, of radius r_c. The number of rods per unit area of the plane perpendicular to rods is $1/(\pi r_c)^2$. In the case of plates, the boundary of the unit cell consists of two planes parallel to the nuclear matter slab, at distance r_c from the slab symmetry plane. For the phases of spherical nuclei (3N), nuclear matter rods (2N) and plates (1N) one obtains then

$$\mathcal{E}_C = \frac{4\pi}{5} \left(n_{p,i} e r_p\right)^2 f_d(w) \ , \tag{22}$$

where

$$f_d(w) = \frac{5}{(d+2)} \left[\frac{1}{d-2} \left(1 - \frac{1}{2} d w^{1-2/d} \right) + \frac{1}{2} w \right] \ . \tag{23}$$

In the case of $d = 2$ (rods) one has to take the limit of $d \longrightarrow 2$, in order to get a more familiar expression

$$f_2(w) = \frac{5}{8} \left(\ln \frac{1}{w} - 1 + w \right) \ . \tag{24}$$

These formulae hold also in the case of the neutron gas tubes (2B) and neutron gas bubbles (3B) but one has then to replace w by $1 - w$. Of course, r_p is then the radius of the tubes or the bubbles.

The virial theorem, which states that in equilibrium $\mathcal{E}_{N,surf} = 2\mathcal{E}_{Coul}$, remains valid for any phase. It is a consequence of scaling of the Coulomb and surface energy density with respect to the value of r_p ($E_{N,surf} \propto r_p^{-1}$, $E_C \propto r_p^2$), and simultaneous invariance in the case of $d = 2$ and $d = 1$ with respect to the change of the scale in the remaining one and two dimensions. In the case of bubbular phases (bubbles, tubes), one has to replace w by $1 - w$.

Beautiful simplicity of the formulae is lost when one introduces "curvature corrections" to the finite-size terms. In the case of the surface terms, they result from the fact that the energy of the nuclear surface depends on its curvature, which in the case of the five nuclear shapes under consideration is given by $\kappa = (d-1)/r_p$ for the phases 3N, 2N and $\kappa = -(d-1)/r_p$ for the 3B, 2B ones, respectively. Surface thermodynamic potential, calculated including lowest order curvature correction, is then given by $\sigma = \sigma_s + \kappa\sigma_c$. It should be stressed, that in contrast to *surface tension* σ_s, the *curvature tension* σ_c does depend on the choice of the "reference surface", which in our case is taken at $r = r_p$ (see, e.g., [48], [30]). In the case of the Coulomb energy, curvature corrections appear when we include the diffuseness of the proton surface. These corrections were studied in detail by Lorenz [54](see also [29]).

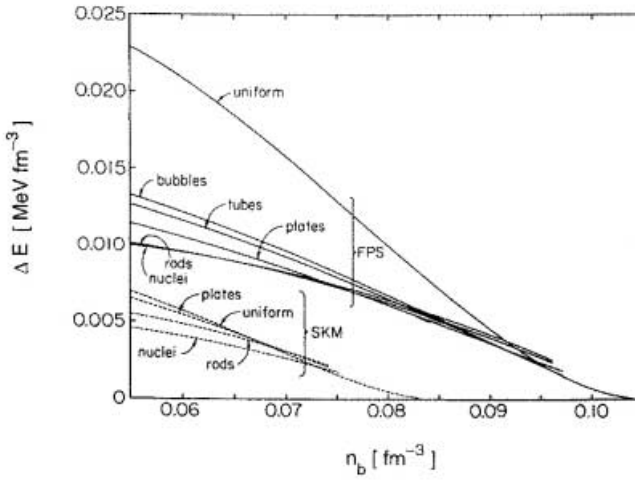

Fig. 7. Energy density of a given phase of inner-crust matter minus that of the bulk two-phase nuclear matter-neutron gas-electron gas system, as a function of the average baryon density $n_{\rm b}$. Label "uniform" corresponds to the case of the uniform *npe* matter. Calculations performed for the FPS and SkM effective nucleon-nucleon interactions. After [55].

First detailed calculations of the structure of the inner crust at $\rho \gtrsim 10^{14}$ g cm^{-3}, performed within the CLDM by Lorenz et al. [55], indicated that the presence or absence of unusual nuclear shapes before transition to uniform *npe* matter depends on the assumed model of effective nucleon-nucleon interaction. For the FPS model of effective N-N interaction, they found a sequence of 3N $\longrightarrow$ 2N $\longrightarrow$ 1N $\longrightarrow$ 2B $\longrightarrow$ 3B phase transition, which started at 0.064 fm^{-3} $\simeq \frac{1}{3}n_0$ (1.1×10^{14} g cm^{-3}), and ended at $n_{\rm edge} = 0.096$ fm^{-3} ($\rho_{\rm edge} = 1.6 \times 10^{14}$ g cm^{-3}) with a transition from the 3B phase to uniform *npe* matter. All phase transitions were very weakly first-order, with relative density jump below 1%. It should be stressed that in the relevant density region the differences between $\mathcal{E}(n_b)$ for various shapes is very small and amounts typically to less than 0.001 MeV/fm^3. This is to be compared with $\mathcal{E}({\rm crust; shape}) - \mathcal{E}({\rm uniform}) \simeq 0.01 - 0.02$ MeV/fm^3 (see Fig.7).

As Lorenz et al. [55] have shown, the very presence of unusual shapes depends on the assumed model of $v_{\rm NN}^{\rm eff}$. In the case of the SkM force (used by Bonche and Vautherin [14],[15] in their dense and hot matter studies) spherical nuclei were energetically preferred down to the bottom edge of the crust, found at significantly lower density $n_{\rm edge} = 0.074$ fm^{-3} ($\rho_{\rm edge} = 1.2 \times 10^{14}$ g cm^{-3}).

Further calculations confirmed this unfortunate ambiguity, resulting from dependence on $v_{\rm NN}^{\rm eff}$. Using parameterized density profiles in the ETF energy density functional, Oyamatsu [67] found complete sequence of phase transitions in the

density range $1.0 - 1.5 \times 10^{14}$ g cm^{-3}. Similar sequence of phase transitions was found by Sumiyoshi et al. [87], with however a much narrower range of existence of unusual nuclear shapes, $0.050 - 0.058$ fm^{-3} ($0.83 - 0.97 \times 10^{14}$ g cm^{-3}), before final transition to uniform *npe* matter. On the contrary, Cheng et al. [28], using unconstrained relativistic ETF approach, found that spherical nuclei persist in the ground state of the crust down to $n_{\rm edge}$, which depending on the parameters of their relativistic $\sigma - \omega - \rho$ Lagrangian ranged from 0.058 fm^{-3} to 0.073 fm^{-3}. Similarly, calculations performed by Douchin and Haensel [30] with SLy4 effective N-N force indicated absence of unusual nuclear shapes. They found transition to uniform *npe* matter at $n_{\rm edge} = 0.078$ fm^{-3} ($\rho_{\rm edge} = 1.3 \times 10^{14}$ g cm^{-3}).

While the presence of unusual nuclear shapes for $\rho \lesssim \rho_{\rm edge}$ depends on effective nuclear interaction model used, some general qualitative statements, based on existing calculations, can still be made. The very phenomenon of phase transitions between various shapes results from the interplay of three quantities: finite-size (surface and Coulomb) term in $E_{\rm cell}$, the dominating bulk energy term, and the volume fraction of the denser nucleon fluid, w. If finite-size terms are small, then $\rho_{\rm edge}$ is reached at relatively low value of w. However, unusual (non-spherical) shapes become energetically advantageous only at sufficiently large value of w. Therefore, small surface tension may prohibit the appearance of unusual shapes before $\rho_{\rm edge}$ is reached (this is the case of the SLy4 and SkM forces. It should be stressed, however, that phase transitions themselves result from very small energy differences (see Fig. 7) of energy densities: finite-size terms in the relevant density range are very small compared to $E_{\rm bulk} = E_{\rm N,bulk} + E_e$.

In the case of the CLDM, one should stress very important role of the curvature term in $E_{\rm N,surf}$, which should therefore be included in any CLDM calculations of the crust-liquid core transition. As we already mentioned, introducing curvature corrections in the finite-size terms complicates the analysis of the unusual shape problem. In the absence of the curvature correction to $E_{\rm N,surf}$, it is possible to show that the 3N$\longrightarrow$2N transition has to occur at $w = 0.2$ [66]. However, in the presence of the curvature correction the 3N phase can persist at larger values of w.

In actual CLDM or ETF calculations, the change of nuclear shape in the ground state of the inner crust is accompanied by a very small (less than one percent) density jump; it has therefore the character of a very weak first-order phase transition [55],[67],[87]. The equation of state in the region in which the nuclear shape transitions occur is obtained using Maxwell construction at the transition pressures.

The CLDM model is *par excellence* classical. Also, the ETF scheme is a semiclassical approximation to a quantum-mechanical many-body problem. As the differences of energy densities between phases with different nuclear shapes are very small, one may worry about possible importance of neglected quantum effects. In the case of terrestrial nuclear physics, there exists a systematic procedure of adding quantum (shell) corrections to the smooth liquid drop model energies of nuclei (Strutinsky method, see, e.g., [74]). Energy correction, resulting from the quantum shell effects for protons, and for various nuclear shapes,

has been calculated by Oyamatsu and Yamada [68]. They found, that with inclusion of proton shell effects changes of nuclear shapes occur at higher densities than those obtained using semiclassical ETF calculation.

Another quantum effect neglected in the CLD or ETF model is pairing of nucleons. However, because of large numbers of nucleons in a unit cell, pairing contribution to the energy is negligible. Larger effects, which clearly need a careful investigation, may result from using the Winger-Seine approximation at $\rho \simeq 10^{14}$ g cm^{-3}.

5.2 Reaching the bottom edge of the crust from the denser side

The method of the determination of the bottom edge of the crust, based on the CLDM of nuclei, requires a very high precision of the calculation of the finite-size contribution term, $E_{\rm N,surf} + E_{\rm coul}$, in $E_{\rm cell}$. One has to construct a CLDM model of the ground state of the inner crust, and then find the density of the crust–liquid core transition from the condition of the thermodynamic phase equilibrium. This method requires that one uses the same nuclear hamiltonian for the crust and for the liquid core phase. It requires also very precise many–body method for the description of nuclear structures within the bottom layers of the crust, which is a rather difficult task (see Fig. 7). Luckily enough, calculations described in the previous subsection show that the crust–liquid core phase transition is *very weakly first–order* (i.e., the relative density jump at the crust-liquid core interface is very small). Therefore, one can locate the crust-core interface using completely different method, which is based on a well known technique used in the theory of phase transitions in condensed matter. This can be an independent test of precision of the CLDM calculation of $\rho_{\rm edge}$, described in the previous subsection. We will locate the edge of the crust by checking the stability of the uniform *npe* matter, starting from the higher density side where we know that the homogeneous phase is indeed stable with respect to formation of spatial inhomogeneities (BBP, Pethick et al. [71]). By lowering the density, we will eventually find the threshold density, at which the uniform *npe* matter becomes unstable for the first time. As we will see, this threshold density gives a very good approximation of the actual density of the crust edge density, $\rho_{\rm edge}$.

At a given n_b, the ground state of a homogeneous *npe* matter corresponds to the minimum of the energy density $\mathcal{E}(n_n, n_p, n_e) = \mathcal{E}_0$, under the constraints of fixed baryon density and electric charge neutrality, $n_p + n_n = n_b$ and $n_e = n_p$, respectively. This implies beta equilibrium between the matter constituents and ensures vanishing of the first variation of $\mathcal{E}$ due to small perturbations $\delta n_j(\mathbf{r})$ (where $j = n, p, e$) of the equilibrium solution (under the constraints of constant total nucleon number and global charge neutrality within the volume V of the system). However, this does not guarantee the stability of the spatially homogeneous state of the *npe* matter, which requires that the second variation of $\mathcal{E}$ (quadratic in δn_j) be positive.

The expression for the energy functional of slightly inhomogeneous neutron-star matter can be calculated using the semi-classical ETF treatment of the kinetic and the spin-gradient terms in nucleon contribution to $\mathcal{E}$ [16]. Assuming

that the spatial gradients are small, we keep only the quadratic gradient terms in the ETF expressions. This approximation is justified by the fact that characteristic wavelengths of periodic perturbations will turn out to be much larger than the internucleon distance. With these approximations, the change of the energy (per unit volume) implied by the density perturbations can be expressed, keeping only second order terms (BBP, [71]),

$$\mathcal{E} - \mathcal{E}_0 = \frac{1}{2} \int \frac{\mathrm{d}\mathbf{q}}{(2\pi)^3} \sum_{j,k} F_{jk}(\mathbf{q}) \delta n_j(\mathbf{q}) \delta n_k(\mathbf{q})^* \ , \tag{25}$$

where we used the Fourier representation

$$\delta n_j(\mathbf{r}) = \int \frac{\mathrm{d}\mathbf{q}}{(2\pi)^3} \delta n_j(\mathbf{q}) \mathrm{e}^{\mathrm{i}\mathbf{q}\mathbf{r}} \ . \tag{26}$$

The Hermitian $F_{ik}(\mathbf{q})$ matrix determines the stability of the uniform state of equilibrium of the *npe* matter with respect to the spatially periodic perturbations of wavevector $\mathbf{q}$. Due to the isotropy of the homogeneous equilibrium state of the *npe* matter, F_{ik} depends only on $|\mathbf{q}| = q$. The matrix elements F_{ik} are calculated from the second variation of the microscopic energy functional $\mathcal{E}[n_n, n_p, n_e, \nabla n_n, \nabla n_p, \nabla n_e]$ (BBP, [71]).

The condition for the F_{ij} matrix to be positive-definite is equivalent to the requirement that the determinant of the F_{ij} matrix be positive (Pethick et al. 1995). At each density n_b, one has thus to check whether $\det[F_{ij}(q)] > 0$. Let us start with some n_b, at which $\det[F_{ij}(q)] > 0$ for any q. By decreasing n_b, we find eventually a wavenumber Q at which stability condition is violated for the first time; this happens at some density n_Q. For $n_b < n_Q$ the homogeneous state is no longer the ground state of the *npe* matter since it is unstable with respect to small periodic density modulations.

Calculations performed with several effective nuclear Hamiltonians indicate that $n_Q \simeq n_{\mathrm{edge}}$, within a percent or better [71],[30]. For the ETF approximation to be correct, the value of the characteristic wavelength of critical density perturbations, $\lambda_Q = 2\pi/Q$, must be significantly larger than the mean internucleon distance. The critical wavenumbers Q are typically ~ 0.3 fm^{-1}. Therefore, despite a small proton fraction (about 3–4% at n_Q), $\lambda_Q \sim 20$ fm is typically four times higher than the mean distance between protons $r_{pp} = (4\pi n_p/3)^{-1/3}$; for neutrons this ratio is typically about eight.

The instability at n_Q signals a phase transition with a loss of translational symmetry of the *npe* matter, and appearance of nuclear structures. The agreement of n_Q and n_{edge} is a good test of the precision of determination of n_{edge}. It implies also that the spherical unit cell approximation for 3N or 3B phases is valid even close to ρ_{edge}. This agreement means also that restriction to linear curvature correction in σ within the CLDM is sufficiently precise. Finally, it is a convincing argument for the validity of the CLDM at very large neutron excess.

6 Formation of accreted crust and crustal non-equilibrium processes

While a newly born neutron star is clearly made of hot matter in nuclear equilibrium, its subsequent evolution can lead to formation of regions in which matter is far from it. Such a situation may take place in the neutron star crust, where the reshuffling of nucleons necessary for the formation of large nuclei characteristic of cold catalyzed matter may be prohibited due to the high Coulomb barriers. This is the case of an old accreting neutron star. For the accretion rate of the order of $10^{-10} M_\odot$/y typical temperature in the neutron star interior does not exceed 10^8 K [34]. Let us consider standard scenario connected with phenomenon of X-ray bursts. Explosive burning of the helium layer leads to formation of matter consisting mainly of ^{56}Ni, which transforms into ^{56}Fe. The growing layer of processed accreted matter pushes down the original crust. The original catalyzed (ground state) outer crust, which consisted of nuclei embedded in electron gas, is replaced by a new, non-catalyzed one in $\sim 10^5$ y. In view of low temperature ($T \lesssim 10^8$K) the only processes which can take place in crystallized matter when it sinks inwards are: electron captures, neutron emission or absorption and, at sufficiently high density, pycnonuclear fusion. Detailed study of the processes taking place in the crust of an accreting neutron star has been done by Sato [83], who considered several scenarios with different initial composition of matter, and by Haensel and Zdunik [37] (see also Bisnovatyi-Kogan and Chechetkin [8], and references therein).

Non-catalyzed neutron star crust represents a source of energy. The energy release takes place due to the non-equilibrium processes in the crust of an accreting neutron star. Some aspects of this problem have been considered by Vartanyan and Ovakimova [89] using an unrealistic model of neutron star matter. Detailed study of non-equilibrium processes, and resulting crustal heating was presented by Haensel and Zdunik [37].

The non-equilibrium processes lead to the appearance of spherical (or more generally - quasi-spherical) surfaces, on which heat is produced at a rate proportional to accretion rate. As Haensel and Zdunik [37] have shown, the resulting total heat release in the solid crust can be larger than the original inward heat flow resulting from the steady hydrogen burning between the helium flashes [34].

6.1 A model of accreted neutron star crust

We assume that at a given pressure, P, the neutron star crust is a body-centered cubic crystal lattice of a single species of atomic nucleus (A, Z), immersed in an electron gas, and, above neutron drip point, also in a neutron gas. The maximum temperature in the crust of accreting neutron star can be as high as 10^8K [34]. Therefore, we can expect that some part of the neutron star crust will be in a liquid phase. While the transport properties of dense matter such as heat conductivity depend sensitively on whether matter is in a liquid or a crystallized phase, melting of the crust introduces only minor corrections to thermodynamic potentials. The latent heat of crystallization is of the order of less than

0.1 keV per one accreted nucleon (c.f.,[49]) and thus negligible. Generally, for $\rho \gtrsim 10^8$ g cm^{-3} and $T \lesssim 10^8$ K thermal contributions to thermodynamic potentials can be safely neglected and the composition and equation of state of dense matter can be calculated using the $T = 0$ K approximation.

In the case of neutron star matter below the helium layer we have $\rho \gtrsim 10^7$ g cm^{-3} and $T \lesssim 10^8$ K and we may therefore calculate all the thermodynamic potentials in the $T = 0$ K approximation. Before the pycnonuclear fusion becomes possible, the unit (W-S) cell contains a fixed number of nucleons, $A_{\rm cell}$, equal to the mass number of the nucleus produced by explosive helium burning. In other words, the number of nuclei in an evolving neutron star matter element is then fixed.

In what follows, we will describe a scenario developed by Haensel and Zdunik [37],[38]. Before the neutron drip point $A_{\rm cell} = A$. At given pressure the equilibrium value of Z is determined from the condition that the Gibbs energy of the unit cell, (2), be minimum. Experimental values of $W_{\mathcal{N}}(A, Z)$ are used whenever they were available. For the nuclei for which no experimental data exist Haensel and Zdunik [37] used a theoretical compressible liquid drop model (CLDM) of Mackie and Baym [56]. A few phenomenological parameters of this model have been fitted to the experimental masses of the atomic nuclei without introducing any shell correction term. Haensel and Zdunik [37], [38] used this model in its original form, which gives the best fit to nuclear masses. Thus, the CLDM formula for $W_{\mathcal{N}}(A, Z)$ includes the phenomenological even - odd pairing term, which makes even-even nuclei more bound, and odd-odd nuclei less bound than the odd-even ones.

Above neutron drip point, $P > P_{\rm ND} \equiv P(\rho_{\rm ND})$, neutrons are present in two phases: bound in nuclei and as a neutron gas outside nuclei. In what follows, we use the formalism and notation applied previously for the determination of the neutron drip point in Sect. 3. The Gibbs energy of the W-S cell is then written in the form

$$\begin{aligned} &G_{\rm cell}(A, Z) = W_{\mathcal{N}}(A, Z, n_n) + W_L(n_{\mathcal{N}}, Z) \\ &+[\mathcal{E}_e(n_e) + (1 - n_{\mathcal{N}} V_{\mathcal{N}})\ \mathcal{E}_n(n_n) + P]/n_{\mathcal{N}}\ , \end{aligned} \tag{27}$$

where $\mathcal{E}_n$ is the energy density of neutron gas (including neutron rest energy) and $V_{\mathcal{N}}$ is the volume of the nucleus. At given (A, Z) the values of $n_{\mathcal{N}},\ n_e,\ n_n$ are determined from the system of three equations,

$$\begin{aligned} P \quad &= P_e(n_e) + P_L(n_{\mathcal{N}}, Z) + P_n(n_n)\ , \qquad n_e = Z n_{\mathcal{N}} \\ A_{\rm cell} &= A + n_n(1/n_{\mathcal{N}} - V_{\mathcal{N}})\ , \end{aligned} \tag{28}$$

supplemented by the condition of mechanical equilibrium of the surface of the nucleus under the external pressure of neutron gas. This last condition, applied to the compressible liquid drop model of Mackie and Baym [56] for $W_{\mathcal{N}}$ which takes into account the influence of the neutron gas on the nuclear surface energy and on the nuclear radius, yields the equilibrium value of $V_{\mathcal{N}}$.

The model described above enables one to calculate, at a given pressure, the ground state of a matter element under an additional constraint of a fixed

number of nuclei. However, we should remind that our task is to follow the ground state of a matter element as it descends deeper and deeper into the neutron star interior under the pressure of accreted matter. This process is taking place at rather low temperature. In practice, this means that matter element sits at the local minimum of $G_{\rm cell}$, and that this local ground state can change only after the corresponding energy barrier vanishes. [4] In view of the characteristic behavior of $W_{\mathcal{N}}$ as a function of A and Z, resulting from the pairing of nucleons in nuclei, this leads to non-equilibrium character of processes which change Z (and A) during the evolution of the neutron star crust.

6.2 Evolution of matter element

In what follows we will study evolution of a matter element with initial density $\sim 10^8$ g cm^{-3}, under a gradual compression up to the density $\sim 10^{13}$ g cm^{-3}, the temperature of matter not exceeding significantly 10^8 K. In order to estimate the timescales for such a compression process, let us consider a 1.4 $M_\odot$ neutron star, with a medium-stiff EOS of the liquid core. Calculation of the density profile of such a neutron star shows, that in order to compress a matter element, initially at $\rho = 10^8$ g cm^{-3}, to the density $\rho = 6 \times 10^{11}$ g cm^{-3}, which as we will see corresponds to the neutron drip point for our specific scenario, the star should accrete a mass of $3 \times 10^{-5} M_\odot$. This would take $3 \times 10^5 / \dot{M}_{-10}$ years, where $\dot{M}_{-10}$ is the accretion rate in the units of $10^{-10} M_\odot$/y. Compression up to 1.2×10^{13} g cm^{-3} (this is maximum density which we will consider) would require accretion of $\sim 5 \times 10^{-4} M_\odot$ and thus would take $\sim 5 \times 10^6 / \dot{M}_{-10}$ years. After such a time the whole outer part of the neutron star crust with $\rho < 1.2 \times 10^{13}$ g cm^{-3} would consist of non-catalyzed matter, studied in the present section.

Let us follow the evolution of an element of matter produced in the explosive helium burning, as it undergoes compression due to accretion of matter onto stellar surface. Let us start with a pressure close to that just below the helium layer. We have there A=56, Z=26. We shall follow possible transformations taking place in the unit cell during its travel to the deep layers of the neutron star crust. For pressures corresponding to $\rho < \rho_1 = 5.852 \times 10^8$ g cm^{-3} the minimum of $G_{\rm cell}$ corresponds to ^{56}Fe. For pressure just above $P_1 = P(\rho_1)$ the minimum is obtained for ^{56}Cr. However, direct transition $^{56}\mathrm{Fe} \rightarrow {}^{56}\mathrm{Cr}$ would require an extremely slow double electron capture.

In view of the extreme slowness of the ee capture $2e^- + {}^{56}\mathrm{Fe} \longrightarrow {}^{56}\mathrm{Cr} + 2\nu_e$, reaction

$$^{56}\mathrm{Fe} + e^- \longrightarrow {}^{56}\mathrm{Mn} + \nu_e \tag{29}$$

must proceed first. With increasing P, the two-step electron capture reactions occur each time when the threshold for a single electron capture is reached,

[4] Strictly speaking, even at $T = 0$ *quantum tunneling* through energy barrier is possible. Therefore, strict condition for the possibility of leaving the local minimum is that the energy barrier becomes sufficiently low (or thin) so that the timescale for tunneling is short compared to matter element compression timescale.

according to a general scheme

$$\begin{aligned}(A,Z)+e^- &\longrightarrow (A,Z-1)+\nu_e\ ,\\ (A,Z-1)+e^- &\longrightarrow (A,Z-2)+\nu_e\ .\end{aligned} \tag{30}$$

Usually, the first step takes place very (infinitesimally) close to the threshold and therefore is accompanied by a very small (infinitesimal) energy release (quasi-equilibrium process). An exception from this rule is the case in which, due to the selection rules, first electron capture must proceed into an excited state of the daughter nucleus. This is the case of reaction (29). Notice, that because of low temperature, the nucleus undergoing an electron capture should always be considered as being in its ground state. If the daughter nucleus is produced in an excited state, then it de-excites by gamma emission before next electron capture. This leads to the heat release $Q_1 = E_{\rm exc}$ per cell. Second electron capture proceeds always in a non-equilibrium way, because P_2 is significantly above the threshold pressure for the electron capture on the odd-odd $(A, Z-1)$ nucleus. Mechanical equilibrium requires that this process takes place at constant pressure, P_2. On the other hand, because of very high thermal conductivity of matter, resulting from the presence of degenerate electrons, and a very slow accretion rate, reactions occur at constant temperature, T. Thus, the total heat release per one W-S cell, accompanying second capture, (30), is given by the change of the Gibbs energy of the cell (chemical potential of the cell), $Q_2 = G_{\rm cell}(A, Z-1) - G_{\rm cell}(A, Z-2)$ (see, e.g., Prigogine [75]). On average, most of the released heat is radiated away by neutrinos, $E_\nu = \frac{5}{6}(\mu_e - \Delta)$, where Δ is the threshold energy for the second (non-equilibrium) electron capture [7].

The effective *deposited in matter* heat release per one unit cell is thus estimated as

$$Q_{\rm cell} \simeq Q_1 + \frac{1}{6}Q_2\ . \tag{31}$$

Generally, $Q_1 \ll Q_{\rm cell}$.

At $\rho_{\rm ND} = 6.11\times10^{11}$ g cm^{-3} neutrons drip out of the nuclei, which are then ^{56}Ar. This process, occurring at constant pressure $P_{\rm ND}$, proceeds in five steps, and is initiated by an electron capture,

$$\begin{aligned}{}^{56}{\rm Ar}+e^- &\longrightarrow {}^{56}{\rm Cl}+\nu_e\ ,\\ {}^{56}{\rm Cl} &\longrightarrow {}^{55}{\rm Cl}+n\ ,\\ {}^{55}{\rm Cl}+e^- &\longrightarrow {}^{55}{\rm S}+\nu_e\ ,\\ {}^{55}{\rm S} &\longrightarrow {}^{54}{\rm S}+n\ ,\\ {}^{54}{\rm S} &\longrightarrow {}^{52}{\rm S}+2n\ .\end{aligned} \tag{32}$$

The whole chain of reactions (which we will call *non-equilibrium process*) can be symbolically written as $^{56}{\rm Ar} \longrightarrow^{52} {\rm S} + 4n - 2e^- + 2\nu_e$.

For $P > P_{\rm ND}$ electron captures induce non-equilibrium neutron emissions, the general rule being that an even number of electron captures is accompanied by emission of an even total number of neutrons. When determining the path the system follows during nuclear transformations one uses a simple rule: if both electron capture and neutron emission are energetically possible, neutron

emission - which is more rapid - goes first. However, in order to calculate the effective heat release we have to consider a detailed sequence of reactions, taking place at the threshold pressure for the first "trigger" reaction of electron capture.

As the element of matter moves deeper and deeper into the neutron star interior, each time the threshold density for the electron capture is crossed, a chain of electron captures and neutron emission follows. While the "trigger" reaction produces virtually no (or very little) energy release, subsequent non-equilibrium transformations lead to a significant heat production, due mainly to the downscattering of neutrons and de-excitation of nuclei. This is possible because emitted neutrons have energies well above the Fermi surface of superfluid neutron liquid.

Due to electron captures, the value of Z systematically decreases. In consequence, the lowering of the Coulomb barrier for the nucleus-nucleus reaction, combined with decrease of the separation between nuclei and a simultaneous increase of the energy of the quantum zero-point vibrations around the lattice sites opens a possibility of pycnonuclear reactions (for an introduction, see [85]).

In their calculation of the pycnonuclear reaction rate per unit volume, $r_{\rm pyc}$, Haensel and Zdunik [37] used the formulae of Salpeter and Van Horn [82] (see [37] for details). The pycnonuclear timescale is defined as

$$\tau_{\rm pyc} = \frac{n_{\mathcal{N}}}{r_{\rm pyc}} \ . \tag{33}$$

The quantity $\tau_{\rm pyc}$ is a sensitive function of Z and of the density, so that the pressure at which pycnonuclear fusion starts can be quite easily pointed out.

The electron capture on ^{40}Mg nucleus, taking place at $\rho = 1.45 \times 10^{12}$ g cm^{-3}, initiates the reaction

$$^{40}{\rm Mg} \longrightarrow ^{34}{\rm Ne} + 6n - 2e^- + 2\nu_e \ . \tag{34}$$

The subsequent pycnonuclear fusion of the ^{34}Ne nuclei ($Z = 10$) takes place on a timescale of months, much shorter than the time needed for a significant compression due to accretion. The fusion reaction can be written symbolically as

$$^{34}{\rm Ne} + ^{34}{\rm Ne} \longrightarrow ^{68}{\rm Ca} \ . \tag{35}$$

After the pycnonuclear fusion has been completed, the number of nuclei is decreased by a factor of two. Further evolution of the element of matter takes place at a fixed number of nucleons in the unit cell, doubled with respect to the initial one, $A_{\rm cell} = 112$. Pycnonuclear fusion is accompanied by a significant energy release in the form of the excitation energy of the final nucleus. The energy release resulting from pycnonuclear fusion represents an important source of heat within the crust. Results concerning the energy release will be presented in the next subsection.

Table 2. Non-equilibrium processes in the outer crust. Temperature effects are neglected. P and ρ are the threshold pressure and density for reactions initiated by the electron capture. Relative density jump at the threshold pressure is denoted by $\Delta\rho/\rho$. Last two columns give the total energy release, $q_{\rm tot}$, and heat deposited in matter, q, both per one accreted nucleon, accompanying non-equilibrium reactions. After [37].

P (dyn cm^{-2})	ρ (g cm^{-3})	process	$\Delta\rho/\rho$	$q_{\rm tot}$ (MeV)	q (MeV)
7.23 10^{26}	1.49 10^{9}	$^{56}{\rm Fe} \rightarrow ^{56}{\rm Cr} - 2e^- + 2\nu_e$	0.08	0.04	0.01
9.57 10^{27}	1.11 10^{10}	$^{56}{\rm Cr} \rightarrow ^{56}{\rm Ti} - 2e^- + 2\nu_e$	0.09	0.04	0.01
1.15 10^{29}	7.85 10^{10}	$^{56}{\rm Ti} \rightarrow ^{56}{\rm Ca} - 2e^- + 2\nu_e$	0.10	0.05	0.01
4.78 10^{29}	2.50 10^{11}	$^{56}{\rm Ca} \rightarrow ^{56}{\rm Ar} - 2e^- + 2\nu_e$	0.11	0.05	0.01
1.36 10^{30}	6.11 10^{11}	$^{56}{\rm Ar} \rightarrow ^{52}{\rm S} + 4n - 2e^- + 2\nu_e$	0.12	0.06	0.05

Table 3. Non-equilibrium processes in the inner crust. Notation as in Table 2. Neutron fraction in the total number of nucleons, in the layer just above the reaction surface, is denoted by X_n. After [37].

P (dyn cm^{-2})	ρ (g cm^{-3})	process	X_n	$\Delta\rho/\rho$	q (MeV)
1.980 10^{30}	9.075 10^{11}	$^{52}{\rm S} \rightarrow ^{46}{\rm Si} + 6n - 2e^- + 2\nu_e$	0.07	0.13	0.09
2.253 10^{30}	1.131 10^{12}	$^{46}{\rm Si} \rightarrow ^{40}{\rm Mg} + 6n - 2e^- + 2\nu_e$	0.18	0.14	0.10
2.637 10^{30}	1.455 10^{12}	$^{40}{\rm Mg} \rightarrow ^{34}{\rm Ne} + 6n - 2e^- + 2\nu_e$	0.39	0.16	0.12
3.204 10^{30}	1.951 10^{12}	$^{34}{\rm Ne} + ^{34}{\rm Ne} \rightarrow ^{68}{\rm Ca}$			
		$^{68}{\rm Ca} \rightarrow ^{62}{\rm Ar} + 6n - 2e^- + 2\nu_e$	0.39	0.09	0.40
3.216 10^{30}	2.134 10^{12}	$^{62}{\rm Ar} \rightarrow ^{56}{\rm S} + 6n - 2e^- + 2\nu_e$	0.45	0.09	0.05
3.825 10^{30}	2.634 10^{12}	$^{56}{\rm S} \rightarrow ^{50}{\rm Si} + 6n - 2e^- + 2\nu_e$	0.50	0.09	0.06
4.699 10^{30}	3.338 10^{12}	$^{50}{\rm Si} \rightarrow ^{44}{\rm Mg} + 6n - 2e^- + 2\nu_e$	0.55	0.09	0.07
6.044 10^{30}	4.379 10^{12}	$^{44}{\rm Mg} \rightarrow ^{36}{\rm Ne} + 8n - 2e^- + 2\nu_e$			
		$^{36}{\rm Ne} + ^{36}{\rm Ne} \rightarrow ^{72}{\rm Ca}$			
		$^{72}{\rm Ca} \rightarrow ^{66}{\rm Ar} + 6n - 2e^- + 2\nu_e$	0.61	0.14	0.28
7.233 10^{30}	5.665 10^{12}	$^{66}{\rm Ar} \rightarrow ^{60}{\rm S} + 6n - 2e^- + 2\nu_e$	0.70	0.04	0.02
9.238 10^{30}	7.041 10^{12}	$^{60}{\rm S} \rightarrow ^{54}{\rm Si} + 6n - 2e^- + 2\nu_e$	0.73	0.04	0.02
1.228 10^{31}	8.980 10^{12}	$^{54}{\rm Si} \rightarrow ^{48}{\rm Mg} + 6n - 2e^- + 2\nu_e$	0.76	0.04	0.03
1.602 10^{31}	1.127 10^{13}	$^{48}{\rm Mg} + ^{48}{\rm Mg} \rightarrow ^{96}{\rm Cr}$	0.79	0.04	0.11
1.613 10^{31}	1.137 10^{13}	$^{96}{\rm Cr} \rightarrow ^{88}{\rm Ti} + 8n - 2e^- + 2\nu_e$	0.80	0.02	0.01

6.3 Non-equilibrium processes and crustal heating

Detailed results describing the non-equilibrium reactions in the crust of an accreting neutron star are shown in Tables 2, 3. In Table 2 we show results for the outer neutron star crust, where matter consists of nuclei immersed in electron gas. Non-equilibrium electron captures generate heat on the spherical surfaces

(actually: in very thin shells) at pressures indicated in the first column of Table 2. The density of matter just above the reaction surface is given in the second column. Density of matter undergoes a jump at the reaction surface. This results from the fact that reactions take place at a constant pressure, $P \simeq P_e$, which is determined mainly by the electron density $n_e = Zn_{\mathcal{N}}$. At constant pressure, a decrease in Z, implied by the double electron capture, is thus necessarily accompanied by the baryon density and mass density increase, with $\Delta\rho/\rho \simeq 2/(Z-2)$.

In the fifth column of Table 2 we give the total heat release in a unit cell, accompanying a non-equilibrium reaction, divided by the number of nucleons in the cell. As we have shown in the previous subsection, on average only $\sim \frac{1}{6}$ of this heat is deposited in matter, the remaining part being radiated away with neutrinos. In the last column we give the effective (deposited in matter) heat per nucleon in a non-equilibrium process, q. In the steady thermal state of an accreting neutron star, effective heat release per unit time on the i-th reaction surface, Q_i, is proportional to the mass accretion rate, $\dot{M}$. This relation can be written in a suitable form

$$Q_i = 6.03 \cdot \left(\frac{\dot{M}}{10^{-10} M_\odot/\mathrm{y}} \right) \cdot \left(\frac{q_i}{1\ \mathrm{MeV}} \right) 10^{33}\ \mathrm{erg/s}\ . \tag{36}$$

Let us notice that the heat release on the neutron drip surface exceeds the total remaining heat release in the outer crust. This is due to the fact that non-equilibrium neutron emission represents a very efficient channel of matter heating.

In Table 3 we collected results referring to the inner crust of accreting neutron star. The fraction of nucleons in the neutron gas phase is denoted by X_n and refers to the crust shell laying just above the reaction surface. For the sake of simplicity, the description of non-equilibrium processes is largely symbolic.

Results presented in Table 3 show that when a chain of non-equilibrium processes includes pycnonuclear fusion, heat production may be more than an order of magnitude larger than in the case involving only electron captures and neutron emission.

For $\rho > 1.2\ 10^{13}$ g cm^{-3} the energy release per nucleon, due to non-equilibrium processes, is rather small compared to that in the $\rho_{\mathrm{ND}} < \rho < 1.2\ 10^{13}$g cm^{-3} layer. To some extent this is due to the fact that atomic nuclei immersed in a dense neutron gas contain then only a small fraction of the total number of nucleons. On the other hand, being more and more neutron rich, these nuclei become less and less dense and less and less bound.

The validity of the Haensel and Zdunik [37],[38] model becomes questionable at the densities a few times 10^{13}g cm^{-3}. However, one may expect that at such a high density properties of non-catalyzed matter become rather simple. Calculation shows, that if a matter element produced originally in a helium flash could reach a density $\sim 10^{14}$g cm^{-3}, we should expect it to contain only $\sim 10\%$ of nucleons bound in atomic nuclei. In view of this, pressure of matter in the shells of constant (A, Z) (as well as many other properties) at this (and higher) density may be expected to be dominated by non-relativistic neutrons.

6.4 Astrophysical consequences

Non-catalyzed matter in the crust of an accreting neutron stars turns out to be an important reservoir of energy, which is partly released in the non-equilibrium reactions involving electron captures, neutron emissions and pycnonuclear fusion. The total heat release due to non-equilibrium reactions in the neutron star crust is larger than a typical inward heat flow produced by the steady thermonuclear burning of accreted matter between the helium flashes. Detailed calculations of the steady thermal state of neutron stars, accreting at rates $10^{-11} \lesssim \dot{M}/(\mathrm{M}_\odot/\mathrm{y}) \lesssim 10^{-9}$, taking due account of non-equilibrium heat sources in the crust, and with various models of neutron star core, were performed in [58].

Many neutron stars in close X-ray binaries are transient accretors (transients). Such neutron stars exhibit X-ray outbursts separated by long periods (months or even years) of quiescence. It is believed that quiescence corresponds to a low-level, or in extreme case halted, accretion onto neutron star. During high-accretion episodes, heat is deposited by non-equilibrium processes in the deep layers ($10^{12} - 10^{13}$ g cm^{-3}) of accreted crust. This has been shown to be possible mechanism to maintain temperature of neutron star interior sufficiently high to explain thermal X-ray radiation in quiescence [17],[80].

7 Composition of accreted crust

Many neutron stars may have accreted crust. For example, consider the millisecond pulsars. They are thought to be old neutron stars, spun up by the accretion, via an accretion disk, of $\sim 0.1 M_\odot$ from their companion in a close binary system (see, e.g., [44]). Clearly, if such scenario is correct, the whole crust of a typical millisecond pulsar is built of accreted, non-catalyzed matter.

Composition of accreted crust in the "single nucleus" approximation, discussed in detail in the preceding section, was calculated by Haensel and Zdunik [38]. These authors used the same compressible liquid drop model of nuclei as that applied in their study of non-equilibrium processes in accreting crust. In Table 4 we list the nuclides present in the crust of an accreting neutron star. In the third, fourth and fifth columns we give the maximum pressure, $P_{\max}$, mass density, $\rho_{\max}$, and baryon density, $n_{b,\max}$, at which the nuclide is present. In the sixth column we give the value of the electron chemical potential (including rest energy), μ_e, at this density. The fraction of nucleons in the neutron gas phase within the layer ending at $P_{\max}$, denoted by X_n, is shown in the seventh column. Transition to the next nuclide is accompanied by a density jump. In the last column of Table 4 we give the corresponding relative density increase, $\Delta\rho/\rho$. To a very good approximation we have $\Delta n_b/n_b \simeq \Delta\rho/\rho$. Relative density jumps are significantly larger than those in the case of cold catalyzed matter, and exceed 10% above neutron drip point.

As one sees from Table 4, composition of the crust of an accreting neutron star is vastly different from that of a standard neutron star composed of the

catalyzed matter. In the case of an accreting neutron star the value of Z is typically $\lesssim 20$, to be compared with $Z = 40 - 50$ for the cold catalyzed matter above the neutron drip point. At $\rho \simeq 10^{13}$ g cm^{-3} the mass number of nuclei in the accreted crust is about 60, to be compared with about 200 in cold catalyzed matter of the same density. The neutron drip occurs at a similar density as in the cold catalyzed matter. At the highest density considered, $\rho \simeq 1.2\ 10^{13}$ g cm^{-3}, more than 80% of nucleons form neutron gas outside nuclei. The neutron gas gives there a dominating contribution to the pressure. Another remark to be made is that composition given in Table 4 corresponds to an idealized scenario of formation of accreted crust. Possible deviations from this idealized picture are discussed in Sec.10.

An important remark concerns the values of Z. The mean charge of nuclei in the crust of an accreting neutron star turns out to be less than half of that characteristic of the cold catalyzed matter. As pointed out by Sato [83], this will result in a significant reduction of the shear modulus of the crust (see Sect. 9).

8 Equation of state of the neutron star crust

The equation of state (EOS) constitutes an essential input for the calculation of the neutron star models. In the present Section, we discuss the EOS of the outer and inner neutron star crust. Two basic models, corresponding to different idealized scenarios of crust formation, will be considered. First model will be based on the ground state approximation, in which the crust is assumed to be built of cold catalyzed matter (structure of the crust in this approximation was discussed in Sections 3, 4, 5). Then we will describe the EOS of accreted crust, assuming formation scenario described in Sect.6, where the structure of the outer and inner crust was derived within the "single nucleus" approximation.

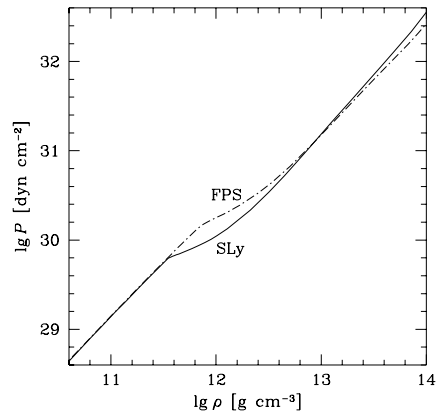

Fig. 8. Comparison of the SLy and FPS EOS.

8.1 Ground state approximation

The EOS of the outer crust in the ground state approximation is rather well established. Generally, the EOS of Haensel and Pichon [39] is quite similar to the more than two decades older BPS EOS [4]. In some pressure intervals one notices a few percent difference between densities, resulting from the difference in the nuclides present at the same pressures.

As soon as one leaves the region of experimentally known nuclei, the EOS of cold catalyzed matter becomes uncertain. This uncertainty rises above the neutron drip density, where only theoretical models can be used. The properties of nuclei become influenced by the outside neutron gas, which contributes more and more to the total pressure. Therefore, the problem of correct modelling of equation of state of pure neutron gas at subnuclear densities becomes important. The real EOS of cold catalyzed matter stems from a real nucleon Hamiltonian, which is expected to describe nucleon interactions at $\rho \lesssim 2\rho_0$ (at higher densities, non-nucleon degrees of freedom, such as hyperons, quarks (?), meson condensates (?), etc., may become relevant). In practice, in order to make the solution of the many-body problem feasible, the task was reduced to that of finding an *effective nucleon Hamiltonian*, which would enable one to calculate reliably the EOS of cold catalyzed matter for 10^{11} g cm$^{-3} \lesssim \rho \lesssim \rho_0$, including therefore the crust-liquid core transition.

Of course, for $\rho \lesssim 4 \times 10^{11}$ g cm^{-3} one can use EOS based on experimental, or semi-empirical nuclear masses, but it is reassuring to check that this EOS is nicely reproduced by a "theoretical EOS", based on an effective nucleon-nucleon interactions FPS and SLy. As one can see in Fig.8, significant differences between the SLy and FPS EOS are restricted to the density interval $4\times10^{11} - 4\times 10^{12}$ g cm^{-3}. They result mainly from the fact that $\rho_{\rm ND}$(SLy) $\simeq 4\times10^{11}$ g cm^{-3}

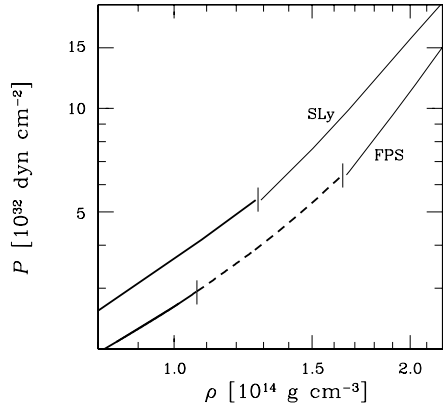

Fig. 9. Comparison of the SLy and FPS EOS near the crust-liquid core transition. Thick solid line: inner crust with spherical nuclei. Dashed line corresponds to "exotic nuclear shapes". Thin solid line: uniform *npe* matter.

Table 4. Composition of the crust of an accreting neutron star. After [38]. For further explanation see the text.

Z	A	$P_{\max}$ (dyn cm^{-2})	$\rho_{\max}$ (g cm^{-3})	$n_{\mathrm{b,max}}$ (cm^{-3})	μ_e MeV	X_n	$\Delta\rho/\rho$ (%)
26	56	$7.235\ 10^{26}$	$1.494\ 10^{9}$	$8.994\ 10^{32}$	4.59	0.00	8.2
24	56	$9.569\ 10^{27}$	$1.1145\ 10^{10}$	$6.701\ 10^{33}$	8.69	0.00	8.9
22	56	$1.152\ 10^{29}$	$7.848\ 10^{10}$	$4.708\ 10^{34}$	16.15	0.00	9.8
20	56	$4.747\ 10^{29}$	$2.496\ 10^{11}$	$1.494\ 10^{35}$	22.99	0.00	10.9
18	56	$1.361\ 10^{30}$	$6.110\ 10^{11}$	$3.651\ 10^{35}$	29.89	0.00	12.1
16	52	$1.980\ 10^{30}$	$9.075\ 10^{11}$	$5.418\ 10^{35}$	32.78	0.07	13.1
14	46	$2.253\ 10^{30}$	$1.131\ 10^{12}$	$6.748\ 10^{35}$	33.73	0.18	14.4
12	40	$2.637\ 10^{30}$	$1.455\ 10^{12}$	$8.682\ 10^{35}$	34.85	0.29	17.0
20	68	$2.771\ 10^{30}$	$1.766\ 10^{12}$	$1.054\ 10^{36}$	34.98	0.39	8.3
18	62	$3.216\ 10^{30}$	$2.134\ 10^{12}$	$1.273\ 10^{36}$	35.98	0.45	8.6
16	56	$3.825\ 10^{30}$	$2.634\ 10^{12}$	$1.571\ 10^{36}$	37.10	0.50	9.0
14	50	$4.699\ 10^{30}$	$3.338\ 10^{12}$	$1.990\ 10^{36}$	38.40	0.55	9.3
12	44	$6.044\ 10^{30}$	$4.379\ 10^{12}$	$2.610\ 10^{36}$	39.92	0.61	13.8
18	66	$7.233\ 10^{30}$	$5.665\ 10^{12}$	$3.377\ 10^{36}$	39.52	0.70	4.4
16	60	$9.2385\ 10^{30}$	$7.041\ 10^{12}$	$4.196\ 10^{36}$	40.85	0.73	4.3
14	54	$1.228\ 10^{31}$	$8.980\ 10^{12}$	$5.349\ 10^{36}$	42.37	0.76	4.0
12	48	$1.602\ 10^{31}$	$1.127\ 10^{13}$	$6.712\ 10^{36}$	43.41	0.79	3.5
24	96	$1.613\ 10^{31}$	$1.137\ 10^{13}$	$6.769\ 10^{36}$	43.55	0.79	1.5
22	88	$1.816\ 10^{31}$	$1.253\ 10^{13}$	$7.464\ 10^{36}$	43.69	0.80	....

(in good agreement with the "empirical EOS" of [39]), while $\rho_{\mathrm{ND}}(\mathrm{FPS}) \simeq 6 \times 10^{11}$ g cm^{-3}. For 4×10^{12} g cm$^{-3} \lesssim \rho \lesssim 10^{14}$ g cm^{-3} the SLy and FPS EOS are very similar, with the FPS EOS being a little softer at highest densities. Detailed behavior of two EOS near crust-liquid core transition can be seen in Fig.9. The FPS EOS is softer than the SLy one.

In the case of the SLy EOS the crust-liquid core transition takes place as a very weak first-order phase transition, with relative density jump of the order of a percent. Let us remind that for this model spherical nuclei persist down to the bottom edge of the crust. As one can see in Fig.9, crust-core transition is accompanied by a noticeable jump of the slope (stiffening) of the EOS. For the FPS EOS, the crust-core transition takes place through a sequence of phase transitions with changes of nuclear shapes. These phase transitions make the crust-core transition smoother than in the SLy case, with a gradual increase of stiffness, which nevertheless suffers a visible jump at the bottom of the bubble-layer edge. All in all, while presence of exotic nuclear shapes is expected to have dramatic consequences for the transport, neutrino emission, and elastic properties of neutron star matter, their effect on the EOS is rather small.

The SLy EOS of the crust, calculated including adjacent segments of the liquid core and the outer crust, is shown in Fig.10. In the outer crust segment, the SLy EOS cannot be graphically distinguished from that of Haensel and Pichon [39], which was based on experimental nuclear masses.

8.2 Accreted crust

Equation of state of accreted crust was calculated by Haensel and Zdunik [38], within the "single nucleus" scenario, described in preceding subsection. This EOS is compared with SLy model of cold catalyzed matter in Fig. 11. Up to neutron drip point, both equations of state are quite similar. This is easily understood: for $\rho < \rho_{\rm ND}$ we have $P \simeq P_e$, which in turn depends only the ratio Z/A, quite similar for both accreted and ground state EOS.

Significant differences appear for $\rho_{\rm ND} \lesssim \rho \lesssim 10\rho_{\rm ND}$, where EOS of accreted matter is stiffer than that of cold catalyzed matter. Also, one notices well pronounced constant-pressure density jumps in EOS of accreted matter, which are due to discontinuous changes in nuclear composition. These density jumps, accompanying first order phase transitions, are particularly large for $\rho_{\rm ND} \lesssim \rho \lesssim 10\rho_{\rm ND}$, and lead to an overall softening of the EOS of accreted crust. For $\rho \gtrsim 10^{13}$ g cm^{-3} EOS for accreted crust becomes very similar to that of cold catalyzed matter. The EOS of accreted crust is given in the density interval from $\sim 10^8$ g cm^{-3} to $\rho \simeq 1.5 \times 10^{13}$ g cm^{-3}. The lower limit corresponds to

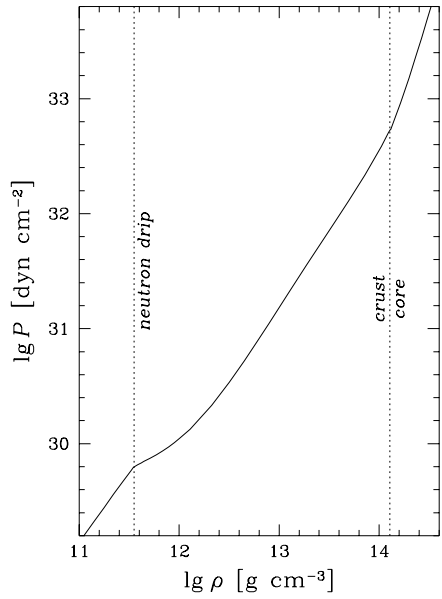

Fig. 10. The SLy EOS. Dotted vertical lines correspond to the neutron drip and crust bottom edge.

the minimum density of the processed accreted matter, just below the bottom of the helium layer (matter is there assumed to be composed of ^{56}Fe). The choice of the upper limit is based on two arguments. Firstly, for $\rho > 10^{13}$ g cm^{-3} our equation of state becomes very similar that of the cold catalyzed matter. Secondly, the validity of the Haensel and Zdunik [38] model of dense matter and, in particular, of the Mackie and Baym [56] model for nuclei, used in their calculations, becomes questionable for the densities much higher than $\sim 10^{13}$ g cm^{-3}.

It is therefore fortunate, that the difference between the cold catalyzed matter and accreted crust equations of state decreases for large density and for $\rho > 10^{13}$ g cm^{-3} both curves are very close to each other. This is due to the fact that for such a high density the equation of state in both cases is determined mainly by the properties of neutron gas. In view of this, the use of the equation of state of the catalyzed matter for the calculation of the hydrostatic equilibrium of the high density ($\rho > 10^{13}$ g cm^{-3}) interior layer of the crust of an accreting neutron star should give a rather good approximation, as far as the density profile is concerned.

9 Elastic properties of neutron star crust

In contrast to the liquid core, solid crust can sustain an *elastic strain*. As neutron stars are relativistic objects, a relativistic theory of elastic media in a curved space-time should in principle be used to describe elastic effects in neutron star structure and dynamics. Such a theory of elasticity has been developed by Carter and Quintana [21] and applied by them to rotating neutron star models in [22],[23]. However, in view of the smallness of elastic forces compared to those of gravity and pressure, we will restrict ourselves, for the sake of simplicity, to the Newtonian version of the theory of elasticity [50].

The state of thermodynamic equilibrium of an element of neutron-star crust corresponds to specific *equilibrium positions* of nuclei, which will be de-

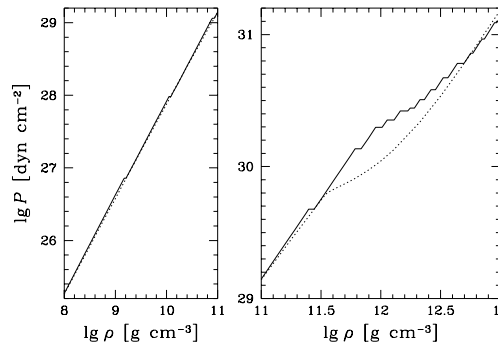

Fig. 11. Comparison of the SLy EOS for cold catalyzed matter (dotted line) and the EOS of accreted crust.

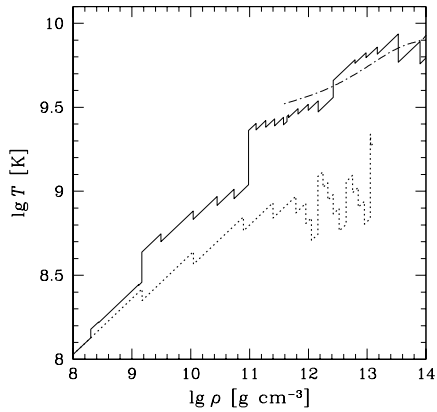

Fig. 12. Melting temperature of neutron star crust versus density. Solid line: Melting temperature for the ground state composition of the crust (Haensel and Pichon [39] for the outer crust and Negele and Vautherin [62] for the inner crust). Jumps at some densities correspond to change of the nuclide. Dash-dotted line: melting temperature of the ground state inner crust, based on the compressible liquid drop model calculation of Douchin and Haensel [30]; its smooth behavior results from dense matter model nature. Dotted line corresponds to the accreted crust model of [38].

noted by $\mathbf{r}$. For pure nuclear composition (one-component plasma) at $T = 0$ and $\rho < 10^{14}$ g cm^{-3}, $\mathbf{r}$ points to the lattice sites of the bcc lattice of nuclei. (Strictly speaking, $\mathbf{r}$ corresponds to *mean* positions of nuclei, which suffer both quantum zero-point, as well as thermal, oscillations.) Neutron star evolution (e.g., spin-down of rotation, cooling) or some outer influence (tidal forces from a close massive body, accretion of matter, electromagnetic strains associated with strong internal magnetic fields) may lead to *deformation* of the crust. In what follows, we will neglect the thermal contributions to thermodynamic quantities and restrict to the $T = 0$ approximation.

Deformation of a crust element with respect to the ground state configuration implies a *displacement* of nuclei into their new positions $\mathbf{r}' = \mathbf{r} + \mathbf{u}$, where $\mathbf{u} = \mathbf{u}(\mathbf{r})$ is the displacement vector. In the continuum limit, relevant for macroscopic phenomena, both $\mathbf{r}$ and $\mathbf{u}$ are treated as continuous fields. Non-zero $\mathbf{u}$ is accompanied by the appearance of *elastic strain* (i.e., forces which tend to return the matter element to the equilibrium state of minimum energy density $\mathcal{E}_0$), and yields *deformation energy* density $\mathcal{E}_{\rm def} = \mathcal{E}(\mathbf{u}) - \mathcal{E}_0$. [5] Uniform translation, described by an $\mathbf{r}$-independent displacement field, does not contribute to $\mathcal{E}_{\rm def}$, and the real (genuine) deformation is described by the (symmetric) *strain tensor*

$$u_{ik} = u_{ki} = \frac{1}{2}\left(\frac{\partial u_i}{\partial x_k} + \frac{\partial u_k}{\partial x_i}\right) , \tag{37}$$

[5] In this section, by "energy" we will always mean energy of a unit volume of matter (i.e., energy density)

where $i, j = 1, 2, 3$, and $x_1 = x,\ x_2 = y,\ x_3 = z$. The above form of u_{ik} is valid when all components of $\mathbf{u}$ are small, and terms quadratic in the components of $\mathbf{u}$ can be neglected compared to the linear ones [50].

Each deformation can be split into *compression* and *shear* components,

$$u_{ik} = u_{ik}^{\rm comp} + u_{ik}^{\rm shear}\ , \tag{38}$$

where

$$u_{ik}^{\rm comp} = \frac{1}{3}{\rm div}\mathbf{u}\ \delta_{ik}\ , \qquad u_{ik}^{\rm shear} = u_{ik} - \frac{1}{3}{\rm div}\mathbf{u}\ \delta_{ik}\ . \tag{39}$$

After a deformation, the volume of a matter element changes according to ${\rm d}V' = (1 + {\rm div}\mathbf{u}){\rm d}V$. Pure compression, which does not influence a shape of matter element, is described by $u_{ik} = a\delta_{ik}$. Pure shear deformation keeps the volume of matter element constant, so that div $\mathbf{u} = 0$.

To lowest order, deformation energy is quadratic in the deformation tensor,

$$\mathcal{E}_{\rm def} = \frac{1}{2}\lambda_{iklm}u_{ik}u_{lm}\ , \tag{40}$$

where summation is assumed over repeated indices. Since deformation energy $\mathcal{E}_{\rm def}$ is a scalar, λ_{iklm} are components of a rank fourth tensor. While the total number of components λ_{iklm} is 81, general symmetry relations reduce the maximum number of linearly independent components (elastic moduli) to 21. The number of independent elastic moduli decreases with increasing symmetry of elastic medium, and becomes as small as three in the case of a bcc crystal, and two in the case of an isotropic solid. Elastic stress tensor, σ_{ik}, is derived from from the deformation energy via $\sigma_{ik} = \partial\mathcal{E}_{\rm def}/\partial u_{ik}$.

9.1 From bcc lattice to isotropic solid

While microscopically the ground state of neutron star crust at $\rho \lesssim 10^{14}$ g cm^{-3} corresponds to a bcc lattice, one usually assumes that its macroscopic properties, relevant for the neutron star calculations, are those of an isotropic bcc polycrystal. Such an assumption is made, because it seems quite probable that neutron star crust is better approximated by a polycrystal than by a monocrystal (see, however, [10]), and also for the sake of simplicity. Elastic properties of an isotropic solid are described by two elastic moduli, and the deformation energy can be expressed as

$$\mathcal{E}_{\rm def} = \frac{1}{2}K({\rm div}\ \mathbf{u})^2 + \mu\left(u_{ik} - \frac{1}{3}\delta_{ik}{\rm div}\ \mathbf{u}\right)^2\ . \tag{41}$$

Here, μ is the *shear modulus* and K is the *compression modulus* of isotropic solid. The stress tensor is then calculated as

$$\sigma_{ik} = \frac{\partial\mathcal{E}_{\rm def}}{\partial u_{ik}} = K{\rm div}\ \mathbf{u}\ \delta_{ik} + 2\mu\left(u_{ik} - \frac{1}{3}{\rm div}\ \mathbf{u}\ \delta_{ik}\right)\ . \tag{42}$$

Considering pure uniform compression one finds that

$$K = n_b \frac{\partial P}{\partial n_b} = \gamma P \ , \tag{43}$$

where γ is the adiabatic index, $\gamma \equiv (n_b/P)\mathrm{d}P/\mathrm{d}n_b$.

Detailed calculations of directionally averaged effective shear modulus of a bcc Coulomb solid, appropriate for the polycrystalline crusts of neutron stars, were performed by Ogata and Ichimaru [65]. These authors considered a one component bcc Coulomb crystal, neglecting screening by the degenerate electrons as well as the quantum zero-point motion of the ions about their equilibrium lattice sites. The deformation energy, resulting from the application of a specific strain u_{ik}, was evaluated directly through the Monte Carlo sampling.

In the case of an ideal bcc lattice there are only three independent elastic moduli, denoted traditionally as c_{11}, c_{12} and c_{44} (see, e.g., [47]). When the crystal is deformed without changing (to lowest order in u_{ik}) the volume of matter element, only two independent elastic moduli are relevant, because

$$\mathcal{E}_{\mathrm{def}} = b_{11}(u_{xx}^2 + u_{yy}^2 + u_{zz}^2) + c_{44}(u_{xy}^2 + u_{xz}^2 + u_{yz}^2), \quad \text{for} \ \ \mathrm{div}\mathbf{u} = 0 \ , \tag{44}$$

with $b_{11} = \frac{1}{2}(c_{11} - c_{12})$. At $T = 0$, Ogata and Ichimaru (1990) find $b_{11} = 0.0245 n_{\mathcal{N}}(Ze)^2/r_{\mathrm{c}}$, $c_{44} = 0.1827 n_{\mathcal{N}}(Ze)^2/r_{\mathrm{c}}$. Significant difference between b_{11} and c_{44} indicates high degree of elastic anisotropy of an ideal bcc monocrystal.

While treating neutron star crust as an isotropic solid is a reasonable approximation (ideal long-range order does not exist there, and we are most prob-

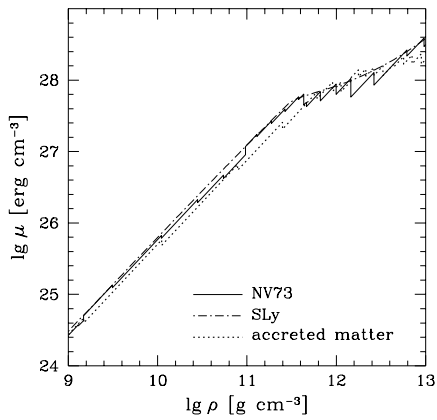

Fig. 13. Effective shear modulus μ versus neutron star matter density, assuming bcc crystal lattice. Solid line - cold catalyzed matter (Haensel and Pichon [39] model for the outer crust, and that of Negele and Vautherin [62] for the inner crust). Dash-dotted line - cold catalyzed matter calculated by Douchin and Haensel [30] (compressible liquid drop model, based on SLy4 effective N-N interaction). Dotted line - accreted crust model of Haensel and Zdunik [38].

ably dealing with a bcc polycrystal), the choice of an "effective" shear modulus deserves a comment. In numerous papers treating the elastic aspects of neutron star dynamics, a standard choice was $\mu = c_{44}$ ([5],[69], [57] and references therein). It is clear, that replacing μ by a single *maximal* elastic modulus of strongly anisotropic bcc lattice is not appropriate. Correct value of μ was calculated by Ogata and Ichimaru [65], who performed directional averages over rotations of the Cartesian axes. At $T = 0$, they obtained (neglecting quantum zero-point oscillations of nuclei)

$$\mu = \frac{1}{5}\left(2b_{11} + 3c_{44}\right) = 0.1194\frac{n_{\mathcal{N}}\left(Ze\right)^2}{r_{\rm c}} \ , \tag{45}$$

nearly two times smaller than $\mu = c_{44}$ used in ([5],[69],[57]). Dependence of μ on temperature was studied, using the Monte Carlo sampling method, by Strohmayer et al. [86]. These authors found that their results can be represented via a simple analytic formula

$$\mu(T) = \frac{\mu(0)}{1 + 1.781\left(100/\Gamma\right)^2} \ , \tag{46}$$

where the ion-coupling parameter $\Gamma = Z^2e^2/(r_{\rm c}k_{\rm B}T)$, and quantum zero-point motion of nuclei has been neglected. Formula (46) fits their numerical results within the estimated numerical error of the Monte Carlo scheme, and reproduces correct $T = 0$ (i.e., $\Gamma = \infty$) limit. As expected, effective shear modulus decreases with increasing temperature.

Let us discuss now qualitative properties of the isotropic neutron star crust. One can easily show, that $\mu \ll K$. This means that neutron star crust is much more susceptible to shear than to compression; its Poisons coefficient $\sigma \simeq 1/2$, while its Young modulus $E \simeq 3\mu$ (for definitions, see [50]).

Strictly speaking, the formulae given in the present subsection hold for the outer crust, where $r_{\mathcal{N}} \ll r_{\rm c}$. They neglect also the effect of the quantum zero-point vibrations of nuclei around their lattice sites. Therefore, in the case of the inner crust these formulae give only an approximation of the actual values of μ.

9.2 Exotic nuclei

Some models of neutron-star matter predict existence of unusual nuclei (rods, plates, tubes, bubbles) in the bottom layer of the crust with $\rho \gtrsim 10^{14}$ g cm^{-3}. Possible structure of this bottom layer was discussed in Sect. 5. In what follows we will concentrate on two specific unusual shapes, namely rods and plates, which are expected to fill most of the bottom crust layer. The properties of matter containing rods and plates are intermediate between those of solids and liquids. For example, displacement of an element of plate matter parallel to the plate plane or rod matter in the direction of rods, is not opposed by restoring forces: this is typical property of a liquid. However, elastic strain opposes any bending of planes or rods, a property specific of a solid. Being intermediate between solids

and liquids, these kinds of matter are usually referred to as *mesomorphic* phases, or *liquid crystals* (see, e.g., [50],[35]). Elastic properties of rod and plate phases of neutron star matter were studied by Pethick and Potekhin [73] (see also [72]).

10 Deviations from idealized models

The ground state crust and accreted crust, described in preceding sections of the present review correspond to idealized perfect one-component plasmas. The real neutron-star crust may be expected to deviate from these idealized models. The practical question to be a asked (and to be answered) is: how much the matter of a real neutron-star crust deviates from a one-component plasma? The knowledge of "imperfections" of the crust is particularly important for its transport properties. The motion of electrons in a significantly disordered ion lattice is qualitatively different from that in a perfect crystal. In the case of a perfect crystal, electrons move in a strictly periodic field, and scatter only on the elementary excitations of the ion lattice - phonons. Disordered ions act as individual scattering centers, strongly limiting electron transport of heat and charge.

10.1 Impurities in a crust of a newly-born neutron star

Initial temperature of the outer layers of a newly born neutron star exceeds 10^{10} K. Under such conditions, nuclear composition of the matter is characterized by some statistical distribution of (A, Z) nuclei in a hot plasma. Initially, the spread in (A, Z) is rather wide [20]. After solidification of the crust its composition is practically frozen, so that it may be expected to reflect the situation at crystallization point rather than in the ground state. In contrast to the ground state composition of the outer crust, at $T \simeq T_{\rm m}$ transitions between shells (A_1, Z_1) and (A_2, Z_2) will be continuous, via a transition layer consisting of a mixture of both nuclides. Only sufficiently far from the transition layer one is dealing with a one-component plasma. Two-component transition layers were studied by De Blasio [11],[12]. The radial width of the transition layers in the outer crust, calculated in [12] for the density range $10^9 - 10^{11}$ g cm^{-3}, was $4 - 12$ m.

10.2 Non-equilibrium neutrons

Higher temperatures are characterized by larger fraction of evaporated nucleons. The most sensitive region is that around the neutron drip point in cold catalyzed matter, $\rho_{\rm ND} \simeq 4 \times 10^{11}$ g cm^{-3}. At $T \simeq 5 \times 10^9$ K, there is a non-negligible fraction of free neutrons for 10^{11} g cm$^{-3} \lesssim \rho \lesssim \rho_{\rm ND}$ (see lower panel of Fig.1). In general, one notices a significant excess of free neutrons for the densities 10^{11} g cm$^{-3} \lesssim \rho \lesssim 10^{12}$ g cm^{-3} as compared to the ground-state composition of the crust. With further cooling, there will be a tendency to absorb these excess neutrons by nuclei, which in turn will increase their A, and modify their Z due

to weak-interaction processes. However, the temperature may be expected to be too low to reach full nuclear equilibrium, mainly because of high Coulomb barriers, and the lack of free protons and α-particles. Therefore, one may expect deviations from the ground-state composition (excess of dripped neutrons) in the cooled crust at 10^{11} g cm$^{-3} \lesssim \rho \lesssim 10^{12}$ g cm^{-3} [8].

10.3 Thermal fluctuations and impurities in the inner crust

General problem of thermal fluctuations of the values of Z and $N_{\rm cell}$ in the inner crust, at $T \simeq T_{\rm m} \gtrsim 10^9$ K, was studied by Jones [46]. Detailed calculations [46], performed within the Compressible Liquid Drop Model, and combined with consideration of the shell and pairing effects, suggest a high degree of heterogeneity in Z to be frozen as the temperature falls below $T_{\rm m}$, with substantial population of two closed Z-shells ($Z = 40$ and $Z = 50$). It should be mentioned that high value of $T_{\rm m}$ (large thermal energies) and large fraction of neutrons (with large fraction of them unbound) in the inner crust are both favorable for impurity fractions higher than those in the outer crust. One has to keep in mind, however, that the kinetics of phase transitions is notoriously difficult for theoretical modelling, especially if approximations used cannot be tested in laboratory. Fortunately, while the "purity" of the crust is of crucial importance for its transport properties, the equation of state is not very sensitive to deviations from the one-nucleus model.

10.4 Impurities in accreted crust

If the ashes of this explosive burning are well approximated by pure ^{56}Fe, then "single-nucleus scenario" described in Sect. 6 may be a valid description. Actually, this is only an approximation; the problem of the detailed outcome of the time-dependent nucleosynthesis during X-ray bursts is very complicated and should be considered as not completely resolved (see, e.g. [78],[84]) The nature of the unstable thermonuclear burning at higher accretion rates 10^{-8} M$_\odot$/y $\lesssim \dot{M} \lesssim 10^{-9}$ M$_\odot$/y is not well understood. The ashes from such a burning might contain some admixture of nuclei beyond the iron group, with $A \simeq 60 - 100$ [84]. Of course, even replacing pure ^{56}Fe by a mix of the iron group elements would substantially complicate the description of the evolution, and would lead to deviation of resulting accreted crust from an idealized model of Sects. 6, 7.

If the starting composition is a mix with significant fractions of different nuclides, one may expect that further evolution will keep heterogeneity of the matter. The thermal and electrical conductivity of such a heterogeneous accreted crust would therefore be drastically lower than that of a perfect crystal. The equation of state would be rather smooth, in contrast to the extreme case of a one-nucleus model with significant density jumps. The values of average Z and A will still be much lower than those characteristic of the ground state of the crust. The number of shells of nonequilibrium processes triggered by electron

captures will be much larger, but the total heat release may be expected to be similar to that estimated in Sect. 6.

10.5 Other scenarios for accreted crust

Up to now, it has been assumed that neutron star accreted baryon mass $M_{\rm b,acc}$ larger than that of initial "primordial crust" composed of catalyzed matter, $M^0_{\rm b,crust}$. In view of the fact that $M^0_{\rm b,crust} \sim 0.01$ M$_\odot$, to reach such a situation at constant accretion rate takes 10^8 years at $\dot{M} = 10^{-10}$ M$_\odot$/y, with required accretion time $\propto (\dot{M})^{-1}$. At earlier times, the crust is composed of an outer layer of accreted and processed matter, of baryon mass $M_{\rm b,acc}$, and an inner layer of baryon mass $M_{\rm b,old} \simeq M^0_{\rm b,crust} - M_{\rm b,acc}$, composed of compressed, processed primordial matter. Evolution of primordial crust under compression due to the weight of accreted layer can be followed shell by shell, with initial ground state composition of the shell. Such a study for a set of several shells with initial density ranging from $10^{8.9}$ g cm^{-3} to $10^{13.6}$ g cm^{-3} was performed by Sato [83].

10.6 Density inversions in accreted crust

They might appear during the evolution of the composition of a "primordial crust" under the weight of accreted layer of matter. In particular, let us focus our attention on the case of the interface between the ^{56}Fe and ^{62}Ni layers. Let us denote the ratio of the density of the upper layer to that of the lower one (at the interface) by $r_{\rm u/l}$. This ratio is initially $r_{\rm u/l} = 0.97$ (see Sect. 3). With increasing pressure, first electron capture take place on ^{56}Fe, $^{56}{\rm Fe} + e^- \longrightarrow {}^{56}{\rm Mn} + \nu_e$, followed by $^{56}{\rm Mn} + e^- \longrightarrow {}^{56}{\rm Cr} + \nu_e$. The interface ^{56}Cr/^{62}Ni is now characterized by the *density inversion* with $r_{\rm u/l} = 1.05$ [9]. In general, density inversions are expected to appear and disappear at various interfaces during compression of primordial crust (Zdunik 2000, unpublished).

Even more significant density inversions may be expected in the case when accretion is very slow, 10^{-16} M$_\odot$/y $\lesssim \dot{M} \lesssim 10^{-12}$ M$_\odot$/y (e.g., accretion of interstellar medium). Under such conditions, temperature within the accreted envelope is so low that helium burning takes place in pycnonuclear regime. It starts with 3α fusion and typically terminates with $^{12}{\rm C}(\alpha,\gamma)^{16}{\rm O}$ reaction [92]. Further compression of the ^{16}O/^{56}Fe interface, accompanied by electron captures, leads to significant density inversions at the evolving interface. However, the timescales needed to reach such situations might exceed 10^{10} yr [9].

If both layers with $r_{\rm u/l} > 1$ were fluid, the interface would be unstable with respect to the Rayleigh-Taylor overturn. However, under typical conditions prevailing at moderate and low accretion rates, $T < T_{\rm m}$ and both layers are solid. In view of this, when analyzing the stability of the interface with respect to perturbations of its shape, one has to include, an addition to pressure and gravity forces, also elastic forces which are opposing the deformation, and might stabilize the interface [9].

Acknowledgements

Results obtained for the SLy interaction, and presented in this review, were obtained with F. Douchin in 1998-2000, and I express my gratitude to him for fruitful collaboration. I am very grateful to D. G. Yakovlev and J. L. Zdunik for reading the preliminary version of this review, critical remarks, and helpful comments. I am also very grateful to A. Y. Potekhin for his help in the preparation of figures.

References

1. J. Arponen: *Nucl. Phys.* **A 191**, 257 (1972)
2. Z. Barkat, J.-R. Buchler, L. Ingber: *Astrophys. J.* **176**, 723 (1972)
3. G. Baym, H.A. Bethe, C. Pethick: *Nucl. Phys.* **A175**, 225 (1971) (**BBP**)
4. G. Baym, C. Pethick, P. Sutherland: *Astrophys. J.* **170**, 299 (1971) (**BPS**)
5. G. Baym, D. Pines: *Ann. Phys. (N.Y.)* **66**, 816 (1971)
6. H.A. Bethe, G. Börner, K. Sato: *Astron. Astrophys.* **7**, 279 (1970)
7. G.S. Bisnovatyi-Kogan, E.F. Seidov,: *Astron. Zh.* **47**, 139 (1970)
8. G.S. Bisnovatyi-Kogan, V.M. Chechetkin: *Uspekhi Fiz. Nauk* **127**, 263 (1979) (English translation: *Sov. Phys. Uspekhi* **22**, 89 (1979))
9. O. Blaes, R. Blandford, P. Madau, S. Koonin: *Astrophys. J.* **363**, 612 (1990)
10. F.V. De Blasio: *Astrophys. J.* **452**, 359 (1995)
11. F.V. De Blasio: *Mon. Not. Roy. Astron. Soc.* **299**, 118 (1998)
12. F.V. De Blasio: *Astron. Astrophys.* **353**, 1129 (2000)
13. J. Boguta, A.R. Bodmer: *Nucl. Phys.* **A 292**, 413 (1977)
14. P. Bonche, D. Vautherin: *Nucl. Phys.* **A 372**, 496 (1981)
15. P. Bonche, D.Vautherin: *Astron. Astrophys.* **112**, 268 (1982)
16. M. Brack, C. Guet, H.-B. Håkansson: *Phys. Rep.* **123**, 275 (1985)
17. E.F. Brown, L. Bildsten, R.E. Rutledge: *Astrophys. J.* **504**, L95 (1998)
18. J.-R. Buchler, Z. Barkat: *Phys. Rev. Letters* **27**, 48 (1971)
19. J.-R. Buchler, Z. Barkat: *Astrophys. Letters* **7**, 167 (1971)
20. A. Burrows, J.M. Lattimer: *Astrophys. J.*, 294 (1984)
21. B. Carter, H. Quintana: *Proc. Roy. Soc. London Ser. A* **331**, 57 (1972)
22. B. Carter, H. Quintana: *Annals of Phys. (N.Y.)* **95**, 74 (1975)
23. B. Carter, H. Quintana: *Astrophys. J.* **202**, 511 (1975)
24. M. Centelles, X. Viñas, M. Barranco, S. Marcos, R.J. Lombard: *Nucl. Phys.* **A 537**, 486 (1992)
25. M. Centelles, X. Viñas, M. Barranco, P. Schuck: *Ann. Phys. (N.Y.)* **221**, 165 (1993)
26. E. Chabanat, P. Bonche, P. Haensel, J. Meyer, R. Schaeffer: *Nucl. Phys.* **A 627**, 710 (1997)
27. E. Chabanat, P. Bonche, P. Haensel, J. Meyer, R. Schaeffer: *Nucl. Phys.* **A 635**, 231 (1998)
28. K.S. Cheng, C.C. Yao, Z.G. Dai: *Phys. Rev.* **C 55 97**, 2092 (1997)
29. F. Douchin, 1999, PhD Thesis, École Normale Supérieure de Lyon, unpublished
30. F. Douchin, P. Haensel: *Phys. Letters* **B 485**, 107 (2000)
31. F. Douchin, P. Haensel, J. Meyer: *Nucl. Phys.* **A 665**, 419 (2000)
32. Ch. Engelmann et al., *Zeitschrift Phys.* **A 352**, 351 (1995)
33. B. Friedman, V.R. Pandharipande: *Nucl. Phys.* **A 361**, 502 (1981)

34. M.Y. Fujimoto, T. Hanawa, I. Iben, Jr., M.B. Richardson: *Astrophys. J* **278**, 813 (1984)
35. P.G. de Gennes, J.Prost, *The physics of liquid crystals*, 2nd ed., Clarendon, Oxford (1993)
36. P. Haensel, J.L. Zdunik, J. Dobaczewski: *Astron. Astrophys.* **222**, 353 (1989)
37. P. Haensel, J.L. Zdunik: *Astron. Astrophys.* **227**, 431 (1990)
38. P. Haensel, J.L. Zdunik: *Astron. Astrophys.* **229**, 117 (1990)
39. P. Haensel, B. Pichon: *Astron. Astrophys.* **283**, 313 (1994)
40. P. Haensel, A.D. Kaminker, D. G. Yakovlev: *Astron. Astrophys.* **314**, 328 (1996)
41. K. Harrison, M. Wakano, J.A. Wheeler, Matter-energy at high density: end point of thermonuclear evolution, in: *La structure et évolution de l'univers*, R. Stoops, Bruxelles, pp.124-140 (1958)
42. B.K. Harrison, K.S. Thorne, M. Wakano, J.A. Wheeler, *Gravitation Theory and Gravitational Collapse*, Chicago University Press, Chicago (1965)
43. M. Hashimoto, H. Seki, M. Yamada: *Prog. Theor. Phys.* **71**, 320 (1984)
44. E.P.J. van den Heuvel, in *IAU Symposium 125, The Origin and Evolution of Neutron Stars*, eds., D.F. Helfand, J.-H. Huang, Reidel, Dordrecht (1987)
45. C.J. Jog, R.A. Smith: *Astrophys. J.* **253**, 839 (1982)
46. P.B. Jones: *Phys. Rev. Letters* **83**, 3589 (1999)
47. C. Kittel, *Introduction to Solid State Physics*, Wiley, New York (1996), Chap. 3
48. K. Kolehmainen, M. Prakash, J.M. Lattimer, J.R. Treiner: *Nucl. Phys. A* **439**, 535 (1985)
49. D.Q. Lamb, H.M. Van Horn: *Astrophys. J.* **200**, 306 (1975)
50. L.D. Landau, E.M. Lifshitz: *Theory of Elasticity*, Pergamon Press, Oxford (1986)
51. W.D. Langer, L.C. Rosen, J.M. Cohen, A.G.W. Cameron: *Astrophys. Space Science* **5**, 259 (1969)
52. J.M. Lattimer, C.J. Pethick, D.G. Ravenhall, D.Q. Lamb: *Nucl. Phys.* **A432**, 646 (1985)
53. J.M. Lattimer, F. Douglas Swesty: *Nucl. Phys.* **A535**, 331 (1991)
54. C.P. Lorenz, PhD Thesis, University of Illinois, unpublished (1991)
55. C.P. Lorenz, D.G. Ravenhall, C.J. Pethick: *Phys. Rev. Letters* **70**, 379 (1993)
56. F.D. Mackie, G. Baym: *Nucl. Phys.* **A 285**, 332 (1977)
57. P.N. McDermott, H.M. Van Horn, C.J. Hansen: *Astrophys. J.* **375**, 679 (1988)
58. J. Miralda-Escudé, P. Haensel, B. Paczyński: *Astrophys. J.* **362**, 572 (1990)
59. P. Möller: 1992, unpublished data, (private communication to B. Pichon, see Haensel and Pichon (1994))
60. P. Möller, J.R. Nix: *Atom. Data Nucl. Data Tables* **39**, 213 (1988)
61. W.D. Myers, W.J. Swiatecki: *Nucl. Phys.* **81**, 1 (1966)
62. J.W. Negele, D. Vautherin: *Nucl. Phys.* **A 207**, 298 (1973)
63. R. Ogasawara, K. Sato: *Prog. Theor. Phys.* **68**, 222 (1982)
64. R. Ogasawara, K. Sato: *Prog. Theor. Phys.* **70**, 1569 (1983)
65. S. Ogata, S. Ichimaru: *Phys. Rev. A* **42**, 4867 (1990)
66. K. Oyamatsu, M. Hashimoto, M. Yamada: *Prog. Theor. Phys.* **72**, 373 (1984)
67. K. Oyamatsu: *Nucl. Phys.* **A561**, 431 (1993)
68. K. Oyamatsu, M. Yamada: *Nucl. Phys.* **A 578**, 181 (1994)
69. V.R. Pandharipande, D. Pines, R.A. Smith: *Astrophys. J.* **208**, 550 (1976)
70. V.R. Pandharipande, D.G. Ravenhall, in: *Proceedings of the NATO Advanced Research Workshop on Nuclear Matter and Heavy Ion Collisions, Les Houches*, ed. by M.Soyeur et al. (Plenum, New York), pp.103 (1989)
71. C.J. Pethick, D.G. Ravenhall, C.P. Lorenz: *Nucl. Phys.* **A 584**, 675 (1995)

72. C.J. Pethick, D.G. Ravenhall: *Annu. Rev. Nucl. Part. Sci.* **45**, 429 (1995)
73. C.J. Pethick, A.Y. Potekhin: *Phys. Lett. B* **427**, 7 (1998)
74. M.A. Preston, R. Bhaduri, *Structure of the Nucleus*, Addison-Wesley Publishing Company, Reading, Massachusetts (1975)
75. Prigogine, *Introduction to Thermodynamics of Irreversible Processes*, Interscience, New York (1961)
76. D.G. Ravenhall, C.D. Bennett, C.J. Pethick: *Phys. Rev. Letters* **28**, 978 (1972)
77. D.G. Ravenhall, C.J. Pethick, J.R. Wilson: *Phys. Rev. Letters* **50**, 2066 (1983)
78. F. Rembges, C. Freiburghans, T. Rauscher, F.-K. Thielemann, H. Schatz, M. Wiescher: *Astrophys. J.* **484**, 412 (1997)
79. P. Ring, P. Schuck: *The Nuclear Many-Body Problem*, Springer-Verlag, New York (1980) (Chapter 13).
80. R.E. Rutledge, L. Bilsten, E.F. Brown, G.G. Pavlov, V.E. Zavlin: *Astrophys. J* **514**, 945 (1999)
81. E.E. Salpeter: *Astrophys. J.* **134**, 669 (1961)
82. E.E. Salpeter, H.M. Van Horn: *Astrophys. J.* **155**, 183 (1969)
83. K. Sato: *Prog. Theor. Phys.* **62**, 957 (1979)
84. H. Schatz, L. Bildsten, A. Cumming, M. Wiescher: *Astrophys. J.* **524**, 1014 (1999)
85. S.L. Shapiro, S.A. Teukolsky, *White Dwarfs, Black Holes, and Neutron Stars*, Wiley, New York (1983)
86. T. Strohmayer, S. Ogata, H. Iyetomi, S. Ichimaru, H.M. Van Horn: *Astrophys. J.* **375**, 679 (1991)
87. K. Sumiyoshi, K. Oyamatsu, H. Toki: *Nucl. Phys.* **A 595**, 327 (1995)
88. S. Tsuruta, A.G.W. Cameron: *Can. J. Phys.* **43**, 2056 (1965)
89. Yu.L. Vartanyan, N.K. Ovakimova, *Soobtcheniya Byurakanskoi Observatorii* **49**, 87 (1976)
90. R.B. Wiringa, V. Fiks, A. Fabrocini: *Phys. Rev. C* **38**, 1010 (1988)
91. R.G. Wolff, PhD Thesis, Technische Universität, München (unpublished) (1983)
92. J.L. Zdunik, P. Haensel, B. Paczyński, J. Miralda-Escudé: *Astrophys. J.* **384**, 129 (1992)